Supplementary Material

Solvent-Dependent Complex Reaction Pathways of Bromoform Revealed by Time-Resolved X-ray Solution Scattering and X-ray Transient Absorption Spectroscopy

Qingyu Kong,[1,2a)] Dmitry Khakhulin,[3] Ilya A. Shkrob,[4] Jae Hyuk Lee,[5] Xiaoyi Zhang,[6] Jeongho Kim,[7] Kyung Hwan Kim,[8] Junbeom Jo,[9,10] Jungmin Kim,[9,10] Jaedong Kang,[9,10] Van-Thai Pham,[1] Guy Jennings,[6] Charles Kurtz,[6] Rick Spence,[6] Lin X. Chen,[4,11] Michael Wulff,[12] and Hyotcherl Ihee[9,10,a)]

[1]*Synchrotron Soleil, L'Orme des Merisiers, St. Aubin 91192 Gif-sur-Yvette, France.*

[2]*School of Physics Science and Information Engineering, Liaocheng University, Shandong Key Laboratory of Optical Communication Science and Technology, Liaocheng University, Liaocheng 252059, China*

[3]*European XFEL GmbH, Holzkoppel 4, D-22869 Schenefeld, Germany.*

[4]*Chemical Sciences and Engineering Division, Argonne National Laboratory, 9700 S. Cass Ave., Argonne, Illinois 60349, USA*

[5]*Pohang Accelerator Laboratory, Pohang 37673, Republic of Korea*

[6]*X-ray Science Division, Argonne National Laboratory, 9700 S. Cass Ave., Argonne, Illinois 60349, USA*

[7]*Department of Chemistry, Inha University, Incheon 22212, Republic of Korea*

[8]*Department of Chemistry, Pohang University of Science and Technology (POSTECH), Pohang 37673, South Korea*

[9]*Department of Chemistry and KI for the BioCentury, Korea Advanced Institute of Science and Technology (KAIST), Daejeon 305-701, Republic of Korea*

[10]*Center for Nanomaterials and Chemical Reactions, Institute for Basic Science (IBS), Daejeon 305-701, Republic of Korea*

[11]*Department of Chemistry, Northwestern University, 2145 Sheridan Rd, Evanston, IL 60208, USA*

[12]*European Synchrotron Radiation Facility, BP 220, F-38043 Grenoble Cedex, France.*

[a)]Author to whom correspondence should be addressed. Electronic mail:kong@synchrotron-soleil.fr; hyotcherl.ihee@kaist.ac.kr

Table of Contents

1. Methods

Materials. Bromoform (99%) and anhydrous methanol (>99.8%) and methylcyclohexane (>99%) were purchased from Sigma-Aldrich and used without further purification.

Time-resolved X-ray liquidography. TRXL data were measured at the ID09B beamline of European Synchrotron Radiation Facility (ESRF). The experimental setup has been described in detail in our previous studies.[1-3] Briefly, the 267 nm laser beam with an energy of 45 μJ/pulse and a pulse width of 1.2 ps was focused to a round spot of 150 × 150 μm^2 to the liquid jet to excite the $CHBr_3$ molecules dissolved in methanol or methylcyclohexane. The nonlinear effect due to multiphoton absorption was evaluated through measuring the solvent peak intensity from laser heating at different excitation energies. The chosen laser energy guarantees a linear and effective excitation. The photoinduced reaction progress was monitored with delayed X-ray pulses of 100 ps duration selected with a synchronized mechanical chopper at a frequency of 986.2 Hz. A pink beam centered at 17.8 keV (0.70 Å) with a flux of 2×10^9 photons per pulse produced from the U17 undulator was focused into a 100×60 μm^2 spot on the sample by a toroidal mirror. A 40 mM solution was circulated through a sapphire nozzle that produced a stable liquid sheet of 300 μm thickness at the flow rate of ~3 m/s. Two-dimensional (2D) X-ray scattering patterns from the sample were collected with an area detector (FReLoN, ESRF) at delay times of –3 ns, –100 ps, 100 ps, 500 ps, 1 ns, 5 ns, 10 ns, 30 ns, 50 ns, 100 ns, 300 ns and 1 μs. Because the photolysis of $CHBr_3$ produces irreversible photoproducts, the sample solution was replaced with a fresh solution every two hours during the experiment to reduce the accumulation of products.

To obtain the solvent heating contribution (green curves in Figures S1 and S7), we performed separate TRXL measurements on solutions of azo-dyes, which do not undergo photoinduced structural change.[4] We used 4-bromo-40-(N,N′-diethylamino)-azobenzene dissolved in methanol and 4-(N,N′-diethylamino)-2-methoxy-40-nitro-azobenzene dissolved in methylcyclohexane at a concentration of 3 mM. The dye solutions were excited at 267 nm, which is the same wavelength used for the photodissociation of $CHBr_3$, and the solvent heating signals for the two solvents were measured.[4]

The measured 2D scattering patterns were integrated azimuthally to obtain one-dimensional scattering curves, $S(q)$, where q is the momentum transfer vector. To extract the structural changes induced by the laser excitation, difference scattering curves, $\Delta S(q)$, were obtained by subtracting the reference scattering curve measured at the time delay of –3 ns (that is,

in the absence of the laser excitation) from the scattering curves measured at positive delay times (that is, in the presence of the laser excitation). The procedure of obtaining the difference scattering curves are described in detail in our previous studies.[1-3] To magnify the scattering intensities at large diffraction angles, the difference scattering curves were multiplied by q, yielding $q\Delta S(q)$.

Time-resolved XAS. XTA data were collected at beamline 11-ID-D of the Advanced Photon Source (APS) at Argonne National Laboratory. A 263 nm laser pulse (50 μJ/pulse, 5 ps fwhm) from the third harmonic output of a Nd:YFL regenerative amplified laser with a repetition of 1.6 KHz was focused to a round spot of 200 × 200 μm^2 to the liquid jet to excite the $CHBr_3$ molecules dissolved in methanol or methylcyclohexane. The X-ray probe pulses were derived from electron bunches extracted from the storage ring with 79 ps fwhm and 6.5 M Hz repetition rate. The progress of the photoinduced reaction was monitored with tunable, monochromatic X-ray pulses. X-ray fluorescence signals were collected using two fast avalanche photodiodes (APDs) that were located in the direction perpendicular to the incident X-ray beam. Solutions of 2 mM $CHBr_3$ in methanol or methylcyclohexane were circulated through a stainless steel tube producing a liquid jet of 550 μm in diameter. The XTA spectra for the photodissociation of $CHBr_3$ were collected at a total of 265 delay times including 120 ps, 5 ns, 50 ns, 100 ns, 153.52 ns, 306.92 ns, 460.32 ns, …, 40.03752 ms (with 153.4 ns time interval from 153.52 ns time delay). Difference X-ray absorption spectra shown in Figures 1c and Figure S5 were obtained by taking the difference between the spectra measured before and after the laser excitation. The experimental setup and data collection are described in detail in previous studies.[5-7]

The time-resolved XAS data for $CHBr_3$ in methanol were collected with delay times of 120 ps, 5 ns, 50 ns and 100 ns after laser excitation. The revolution time of the APS storage ring with a circumference of 1104 m is 3.682 μs, and the time separation between successive X-ray pulses is 153.4 ns in 24-bunch filling mode. All individual X-ray pulses between two successive laser pulses, which were separated by 625 μs (= 1/1.6 kHz), were recorded in our measurement, [6,7] that is, 4074 (= 625 μs/153.4 ns) X-ray pulses after each laser pulse. Extra delay times were obtained by using X-ray pulses coming after the synchronized one. For example, when the time delay between synchronized laser and X-ray pulses was set to be 120 ps, we obtained delay times of 120 ps, 153.4 + 0.12 ns, 306.8 + 0.12 ns… until 625 μs in a single measurement. The actual longest time delay in our measurement was around 40 μs, when the laser-excited solution starts to move out of the probing X-ray spot. As a result, the measured delay times are 120 ps, 5 ns, 50 ns, 100

ns, 153.52 ns, 306.92 ns, 460.32 ns…… till 40037.52 ns, giving a total of 265 delay times. Time-resolved XAS data for $CHBr_3$ in methylcyclohexane were collected in the same way.

Product analyses, kinetics simulations, and magnetic resonance spectroscopy of radicals. The details of these analyses are described in Sections 5 and 6.

DFT calculations. Molecular geometries of putative reaction intermediates and products in solution phase were optimized with density functional theory (DFT) methods implemented in the Gaussian 09 program.[8] The Becke three-parameter hybrid functional[9] with the Lee–Yang–Parr[10] and Perdew–Wang[11] correlation corrections (B3LYP and B3PW91), the 1996 gradient-corrected correlation functional of Perdew, Burke and Ernzerhof (PBE),[12] and the all electron basis set 6-311++G(3df,3pd) for C, H and Br[13] were used for these calculations. The solvent effects were calculated using self-consistent reaction field (SCRF) theory implemented in Gaussian 09, and the continuum polarizable conductor model (CPCM) model[14] was employed to perform geometry optimization in solution. Geometries were fully optimized both in the gas and solution phases. Vibrational frequencies were calculated with analytical second-order derivatives, and zero-point vibrational energies were derived. The number of imaginary frequencies was used to characterize the nature of the optimized structures.

Molecular dynamics (MD) simulations. The solute-solvent interactions (cage structure) for XSS calculations and the solvation shell for XAS calculation were obtained by MD simulations using the MOLDY program.[15] Briefly, the solutes optimized by DFT calculations were placed in a solvent box containing 2048 solvent molecules with the periodic conditions imposed, and the MD simulations were performed up to 2 ns with a step size of 0.5 fs to have better statistics. The averaged radial distribution function, $g(r)$, obtained from the MD simulations were used to calculate the X-ray scattering intensities. Detailed descriptions of the calculation protocol can be found in our previous studies.[2,3] A solvation shell of 10 Å including ~45 methanol or ~15 methylcyclohexane molecules was used for ORCA[16] calculations (see Figure S14), and the XAS spectra were averaged using 10 snapshots sampled every 200 ps along the calculated MD trajectory.

2. Linear combination fitting (LCF)

The experimental TRXL and XTA traces at each delay time were fitted using the linear combination fitting (LCF) algorithm. The theoretical signals were calculated for each solute listed in Table S2 and Figure S2, and their linear combinations were compared with the experimental traces. The strategy was to minimize the figure of merit (χ^2) defined as

$$\chi^2 = \sum_{i=1}^{n} \left(\frac{\Delta S_{theory}(q) - \Delta S_{experiment}(q)}{\sigma_i} \right)^2 \qquad \text{(S1)}$$

where σ_i is the standard deviation at a given time-delay (for a series of repeated measurements) and was indicated as error bars on the experimental curves, and the summation is over the whole q range in a trial set. The concentration changes of various chemical species as a function of delay time is obtained by fitting the experimental data at each time delay separately and plotting the corresponding weights. Although the results obtained from this approach have uncertainties, they allow the identification of a potential kinetic model that can be applied in the global fitting analysis.

3. Global fitting analysis of reaction kinetics

3.1. Kinetic model

To perform full global analysis of the TRXL and XTA data in both methanol and methylcyclohexane we constructed chemical kinetic models based on the results of the extensive LCF analysis as described above and in the main text. The following minimum sets of reactions, RS1 for methanol and RS2 for methylcyclohexane, were selected for the two solvents respectively:

For methanol (RS1):

$CHBr_3 \rightarrow CHBr_2 + Br$ (R1)

$CHBr_3 \rightarrow$ *iso*-$CHBr_2$-Br (R2)

iso-$CHBr_2$-Br + $CH_3OH \rightarrow CH_3OCHBr_2 + HBr$ (R3)

$Br + CHBr_2 \rightarrow CHBr_3$ (R4)

$Br + Br \rightarrow Br_2$ (R5)

$CHBr_2 + Br \rightarrow$ *iso*-$CHBr_2$-Br (R6)

For methylcyclohexane (RS2):

$CHBr_3 \rightarrow CHBr_2 + Br$ (R1)

$CHBr_3 \rightarrow$ *iso*-$CHBr_2$-Br (R2)

$Br + CHBr_2 \rightarrow CHBr_3$ (R4)

$Br + Br \rightarrow Br_2$ (R5)

$CHBr_2 + Br \rightarrow$ iso-$CHBr_{-2}$-Br (R6)

iso-$CHBr_2$-Br $\rightarrow CHBr_3$ (R7)

For methanol, the reaction R3 represents a "chain" reaction in combination with a $CHBr_2$ + Br recombination (R6) or roaming-mediated isomerization (R2) to form *iso*-$CHBr_2$-Br, which then participates in a rapid (<100 ps) solvolysis reaction. Since the temporal resolution of all time-resolved measurements presented in this work is limited by the X-ray pulse duration, which is around 100 ps, the "chain" reaction was considered to occur in one step involving only the reactants and the products, whereas *iso*-$CHBr_2$-Br escaped our detection. Therefore the rate of the formation of CH_3OCHBr_2 is governed solely by the rate of isomer formation, which in turn can occur either via very fast roaming-mediated isomerization (~0.1 ps), fast geminate recombination (< 100 ps), or much slower non-geminate recombination (> 1ns given the concentrations used).

As can be noted, the set of reactions (RS2) for methylcyclohexane is essentially identical to the set of reactions for methanol (RS1), except for the channel associated with the deactivation of *iso-$CHBr_2$-Br*. Indeed, the *iso-$CHBr_2$-Br* has much longer lifetime in methylcyclohexane than in methanol since the solvolysis reaction R3 does not occur in methylcyclohexane. Thus in methylcyclohexane, reaction R7 takes place instead of R3.

To obtain global concentration kinetics for all reaction species including the solvent and the parent bromoform in its ground state, corresponding sets of rate equations describing the reactions (RS1) and (RS2) were constructed.

For methanol (RE1):

$$\begin{cases} \dfrac{dC[CHBr_3]}{dt} = k_{R4} \cdot C[CHBr_2] \cdot C[Br]; \\ \dfrac{dC[Br]}{dt} = -k_{R4} \cdot C[CHBr_2] \cdot C[Br] - k_{R5} \cdot C[Br] \cdot C[Br] - k_{R3} \cdot C[Br] \cdot C[CHBr_2] \cdot C[CH_3OH]; \\ \dfrac{dC[Br_2]}{dt} = \dfrac{1}{2} \cdot k_{R5} \cdot C[Br] \cdot C[Br]; \\ \dfrac{dC[CHBr_2]}{dt} = -k_{R4} \cdot C[CHBr_2] \cdot C[Br] - k_{R3} \cdot C[Br] \cdot C[CHBr_2] \cdot C[CH_3OH]; \\ \dfrac{dC[CH_3OCHBr_2]}{dt} = k_{R3} \cdot C[Br] \cdot C[CHBr_2] \cdot C[CH_3OH]; \\ \dfrac{dC[HBr]}{dt} = k_{R3} \cdot C[Br] \cdot C[CHBr_2] \cdot C[CH_3OH]; \\ \dfrac{dC[CH_3OH]}{dt} = k_{R3} \cdot C[Br] \cdot C[CHBr_2] \cdot C[CH_3OH]; \end{cases}$$

where $C[CHBr_3]$, $C[Br]$, $C[Br_2]$, $C[CHBr_2]$, $C[CH_3OCHBr_2]$, $C[HBr]$, $C[CH_3OH]$ are transient concentrations of the respective species and are corresponding rate constants for the reactions in (RS1).

For methylcyclohexane (RE2):

$$\begin{cases} \dfrac{dC[CHBr_3]}{dt} = k_{R4} \cdot C[CHBr_2] \cdot C[Br] + k_{R7} \cdot C[iso\text{-}CHBr_2\text{-}Br]; \\ \dfrac{dC[Br]}{dt} = -k_{R4} \cdot C[CHBr_2] \cdot C[Br] - k_{R5} \cdot C[Br] \cdot C[Br] - k_{R6} \cdot C[Br] \cdot C[CHBr_2]; \\ \dfrac{dC[Br_2]}{dt} = \dfrac{1}{2} \cdot k_{R5} \cdot C[Br] \cdot C[Br]; \\ \dfrac{dC[CHBr_2]}{dt} = -k_{R4} \cdot C[CHBr_2] \cdot C[Br] - k_{R6} \cdot C[Br] \cdot C[CHBr_2]; \\ \dfrac{dC[iso\text{-}CHBr_2\text{-}Br]}{dt} = -k_{R7} \cdot C[iso\text{-}CHBr_2\text{-}Br] + k_{R6} \cdot C[Br] \cdot C[CHBr_2]; \end{cases}$$

where $C[CHBr_3]$, $C[Br]$, $C[Br_2]$, $C[CHBr_2]$, $C[iso\text{-}CHBr_2\text{-}Br]$ are transient concentrations of the respective species and are corresponding rate constants for the reactions in (RS2).

The *initial conditions*, i.e. the concentrations at *t=0*, were defined according to the results of the LCF analysis. For both solvents the initial concentrations of Br and $CHBr_2$ were put non-zero and equal as the species originating from the same parent molecule. Additionally for the reaction in methanol, the initial concentrations of CH_3OCHB_2, HBr and the reduction of equilibrium molar of methanol (24.699 M) were assumed equal. For the reaction in methylcyclohexane the initial concentration of *iso-$CHBr_2$-Br* was set non-zero. The initial reduction in concentration of the ground state species was then calculated using the law of conservation of mass. Thus for each solvent two groups of species have equal initial concentrations.

For methanol:

$$\underline{\text{group1:}}\ C_{g1} = C_0[Br] = C_0[CHBr_2]$$

$$\underline{\text{group2:}}\ C_{g2} = C_0[CH_3OCHB_2] = C_0[HBr],\ C_0[CH_3OH] = 24.699 - C_{g2}$$

For methylcyclohexane:

$$\underline{\text{group1:}}\ C_{g1} = C_0[Br] = C_0[CHBr_2]$$

$$\underline{\text{group2:}}\ C_{g2} = C_0[\text{iso-}CHBr_2\text{-}Br]$$

thus $C_0[CHBr_3] = C_{gs}[CHBr_3] - (C_{g1} + C_{g2})$ in both cases, where $C_{gs}[CHBr_3]$ is the equilibrium concentration of the solutions before excitation. The initial concentration of the Br_2 species was set to zero.

Two sets of rate equations, (RE1) and (RE2) with initial conditions were solved for the two solvents numerically using the *ode45* function implemented in Matlab® depending on the given set of the reaction rate constants k_i (where i = R3, R4, R5 for methanol and R4, R5, R6, R7 for methylcyclohexane). The resulting kinetics of the reaction species were used for calculating theoretical difference signals for TRXL and XTA as described in the following paragraphs.

3.2. Global optimization for TRXL

In order to perform global optimization of the kinetic parameters for the TRXL data we employed the approach described in detail in the previous report.[3] In brief, the experimental difference scattering signals at different delay times were modelled by the difference scattering patterns of putative intermediates using linear combinations. The model scattering signals arises from three contributions, scattering from the solute, solvent and solute-solvent interactions (cage term). The

solute contribution was computed from DFT-optimized solute structures and the cage term – from MD simulations. Both the experimental and model difference scattering signals were normalized to an electron unit in term of one solvent molecule to obtain absolute concentrations of the excited state species. The solute-related contributions (solute plus cage term) were scaled to one solvent molecule according to the concentration used in the experiment. With 40 mM concentration in methanol, as an example, one solute is surrounded by 618 solvent molecules. The calculated Debye scattering of solute was divided by 618 to match the electron unit of one solvent molecule.

The *solvent-only* contribution in the transient signal is determined using the scattering responses of the solvent to changes in temperature and density triggered by the photochemical reaction. The responses are defined as derivatives of the scattering signal with temperature and density, $\left(\partial S/\partial T\right)_\rho$ and $\left(\partial S/\partial \rho\right)_T$, and were experimentally obtained in an independent measurement by exciting an azo-dye in corresponding solvent as described in the Methods section. The total solvent-only difference signal is then computed using the hydrodynamics formula, $\Delta S_{solvent}(q,t) = \left(\partial S/\partial T\right)_\rho \Delta T(t) + \left(\partial S/\partial \rho\right)_T \Delta\rho(t)$. The time-dependent temperature and density changes are obtained by solving the heat deposition thermodynamics equations according to the energetics of reaction species (see Table S1) and the hydrodynamics equations for the isobaric thermal expansion[1]. In the global analysis of TRXL the reaction kinetics and the thermodynamics of bulk solvent are intrinsically coupled in a self-contained kinetic model allowing for extracting full structural evolution and energetics of the reacting solvated system on the molecular level.

The following parameters were optimized in the global analysis of TRXL data: 1) initial concentrations of several reacting species C_{g1} and C_{g2} (see above); 2) the reaction rate constants k_i (where i = R3, R4, R5 for methanol and R4, R5, R6, R7 for methylcyclohexane); 3) the fraction of the excited molecules, F_{fast}, which relaxes back to the ground state within 100 ps, resulting in instant rise of the solvent temperature.

3.3. Global optimization for XTA

The global optimization of the XTA data was conceptually similar to the TRXL. The model XAS signals of various reacting species were calculated by the ORCA package and the difference XTA signals were obtained by subtracting the reactant from the products (Table S2). Figure S14 shows

the calculated absorption coefficients of the chemical species relevant to the photoreaction in methanol as an example.

In contrast to TRXL, it is difficult to directly extract the absolute concentration of the excited state species from the XTA data, due to the difficulty to scale the XTA data to an electron unit. Therefore the scaling of the difference XTA signals was introduced as a fitting parameter. The scaling amplitude is applied for the entire set of transient curves, as opposed to individual delay times. Additionally, to account for the energy scale uncertainties related to approximations of the theoretical calculation and intrinsic bandwidth of the monochromatic beam, an energy shift parameter ΔE_{XAS} was introduced in the fit and constrained to changes within ± 1 eV.

All global optimization procedures were conducted using the constrained minimizers in the defined sequence of 'interior-point', 'sequential quadratic programming' and 'active-set' optimization algorithms implemented in Matlab® and were performed in at least 2000 iteration steps to ensure full convergence of the optimizers.

The constraints for the fitting parameters were justified solely by the following physical considerations:

1) Molar concentrations of all excited state species were constrained to be always positive and in total not larger than the initial bromoform concentration before excitation;

2) Solvent temperature increase for the TRXL fitting was constrained to be positive;

3) Adjustment of the absolute X-ray photon energy, ΔE_{XAS}, in the XTA fit was constrained to ± 1 eV, according to the approximate spectral bandwidth of the monochromatic beam used in the experiment.

3.4. Individual and combined optimization of TRXL and XTA data

To test robustness of the kinetic models the full sets of experimental TRXL and XTA traces were fitted either independently for each experimental technique or combined in one global optimization procedure using the same set of reaction rate equations and optimized reaction rate constants k_i.

The *independent* fitting for the two techniques was performed by minimizing the chi-squared estimator similar to (S1) for TRXL and XAS separately:

$$\chi^2{}_{XSS/XAS} = \sum\sum\left(\frac{\Delta S_{theory} - \Delta S_{experiment}}{\sigma_i}\right)^2$$

where the double sum is the calculation for all data points of individual traces and then for all delay times of the entire data set. Although the same rate equations were used for both TRXL and XTA, the reaction rate constants were not forced to be equal for the two techniques.

In the *combined* global fitting procedure the rate equations were solved simultaneously for TRXL and XTA per optimization step, thus the reaction rate constants are identical for both data sets. The *combined* optimization was performed by minimizing a sum of two chi-squared estimators χ^2_{XSS} and χ^2_{XAS} resulting from the fitting of TRXL and XTA linked via the reaction constants k_i. To remove potential bias of the optimization towards one technique the respective $\chi^2_{XSS/XAS}$ of the *combined* global fit were normalized to the corresponding minimum $(\chi^2_{XSS/XAS})_{min}$ of the *independent* global, i.e.

$$\chi^2_{comb} = \left(\chi^2_{XSS}/(\chi^2_{XSS})_{min} + \chi^2_{XAS}/(\chi^2_{XAS})_{min}\right)/2$$

In this way the normalized χ^2_{comb} also serves as a measure of the degree of relative discrepancy between the *independent* and the *combined* global analysis approaches, to test the applicability of the chosen global kinetic model describing the XTA and TRXL data sets. In general, the *combined* global optimization represents a fully consistent and complete data analysis framework simultaneously taking advantage of the local element specific sensitivity of XTA and the global structural and thermodynamic sensitivity of TRXL.

3.5. Results of the global analysis

Reaction kinetics of various species and the thermodynamics of bulk solvent were obtained from the combined global analysis in methanol and methylcyclohexane. The reaction kinetics of the transient species and the parent molecule are presented in Figure 5 of the main text, the thermodynamics, i.e. the temperature and density changes as a function of reaction time, are shown in Figure S11. The reaction rate constants, the fraction of molecules relaxing to the ground state within 10 ps, F_{fast}, and the energy shift needed for the XAS fit, ΔE_{XAS}, are shown in Table S5. The χ^2_{comb} in the table demonstrates a very minor discrepancy between sum of squared residuals for the *independent* and the *combined* global analysis within 1.46% and 0.27% for methanol and

methylcyclohexane, respectively, confirming consistency of the model for the two data sets from TRXL and XTA.

Reactions in methanol

According to the results of the global analysis the recombination reaction R4 in methanol is not observed. The main channels are non-geminate recombination (R5) and the solvolysis reaction R3 plus the slow non-geminate recombination of $CHBr_2$ and Br. We note that the final concentration of Br_2 is lower than half of the initial Br concentration, which is reasonable because the Br fragment is additionally consumed in reaction R6 leading to a decrease of the concentration of $CHBr_2$ simultaneously (Figure 5a). The exothermic properties of recombination and solvolysis reactions result in a temperature increase of the solvent after tens of nanoseconds, with the growing rate slows down due to subsequent thermal expansion of the probing volume (Figure S11). The optimization algorithm also returns a relatively high heat release into the solvent within the first 10 ps after excitation that corresponds to roughly 13% of $CHBr_3$ molecules in solution or about half of excited molecules. The concentration evolution obtained from the XTA data demonstrates basically the same kinetics of the species since identical reaction rate constants, which are corrected for lower concentration, are used. As mentioned earlier, the concentration of the excited state species for XTA cannot be directly extracted from the data therefore arbitrary units are shown (Figure 5b).

Reaction in methylcyclohexane

In contrast to the reaction in methanol, the recovery reaction from the isomer to the parent molecule (R7) is allowed in methylcyclohexane by the global optimization algorithm, and the recovery of the parent molecule is thus also displayed in the kinetics plot. By contrast, the recombination rate of Br is much lower due to different mechanism of the fragment-solvent interactions. Although most of the Br is consumed via the direct Br+Br recombination, a small fraction contributes to the reactions of R4 and R6 so that the recovery of the parent species is a sum of R7, R6 and R4. As expected the iso-$CHBr_2$-Br is present in methylcyclohexane solution up to at least 100 ns, and therefore can be detected by TRXL (Figure 5c). Br recombination and isomer relaxation release heat to the solvent, resulting in the increase of the solvent temperature, which decreases as the thermal expansion sets in (Figure S11).

In contrast to the methanol XTA data that represent an irreversible reaction, the amplitude of difference XTA signal in methylcyclohexane decreases over time (Figure S9) illustrating the recovery of the parent bromoform species.

4. Geometric structure refinement

CH_3OCHBr_2: Structure optimization for CH_3OCHBr_2 was performed by fitting the solute-only difference scattering curve at 10 ns, which was obtained by subtracting the solvent related contributions, the cage term and R1 from the total difference TRXL signal (Figure 6a). A symmetry constraint by keeping equivalent CBr and C-Br′ bonds was imposed to simplify the analysis. Three structural parameters were varied: the Br-C (and Br'-C) bond length R, the Br-C-Br' angle ϕ, and the C-O-C angle θ (see insert structure in Figure 6a). The Br-C and Br'-C bond lengths were optimized simultaneously as a single parameter.

In order to evaluate the fitting uncertainties and the correlations among the fit parameters, we calculated the projections of the figure of merit (χ^2) surface onto planes of parameter pairs in the manner described above (Figures. 6c and 6d). Since the strongest contribution in the scattering intensity $S(q)$ comes from the Br-Br interatomic correlations, the Br-C bond length and the Br-C-Br' angle are strongly negatively correlated because the variation of either of the two parameters leads to the variation of the Br-Br' distance (Figure 6c). Much weaker correlations are observed for (R, θ) and (ϕ, θ) pairs (see Figure 6c and Figure S10). This observation reflects smaller contribution of the methyl group to the difference scattering signal and therefore weaker structural sensitivity to the position of CH_3 and larger uncertainty of the C-O-C angle. The optimal values of R, ϕ and θ within the 68% confidence are 2.09 ± 0.02 Å, 102 ± 1°, and 119.8 ± 4°, respectively. The optimal values and experimental errors (at 68% confidence limits) and their comparison with DFT calculations are given in Table 1.

Isobromoform: In a similar manner to CH_3OCHBr_2, we optimized the structure of *iso*-$CHBr_2$-Br using the solute-only difference scattering curve at 100 ps. The structures of $CHBr_3$ and *iso*-$CHBr_2$-Br from DFT calculations were used as input, and the difference scattering signal in q-space was calculated between the Debye scattering of $CHBr_3$ and *iso*-$CHBr_2$-Br with polychromatic correction applied. The structure of the isomer is optimized by varying the Br-Br′ bond length R and the Br′-Br-C angle ϕ (shown in Figure 6e) until the best least-squares fit to the

experimental data is obtained. The third fit parameter, the relative excited state fraction (γ), was introduced because the oscillatory feature in the high q region depends on both the structure and the fraction of photoexcitation. In order to evaluate the uncertainties and the correlations between the fit parameters, we plot the figure of merit (χ^2) contours as projected on the (R, ϕ) and (R, γ) planes of the parameter space near the optimum (Figures 6 g, h). The figure of merit, χ^2, is defined in equation S1. The χ^2 projections were generated by fitting one of the free parameters while the others are iteratively varied on a regular grid of values in the ranges wide enough for defining certain confidence intervals. In this way, the χ^2 value obeys a chi-squared distribution with two degrees of freedom, and the 68% and 95% confidence regions in Figure 6g are defined by the contours where χ^2 increases by 2.3 and 6.14, respectively.[17] Although both pairs of parameters presented in Figures 6g and 6h are strongly correlated, we were able to estimate the uncertainties in the evaluation of the structural parameters, which are ±0.02 Å and ±1° for R and ϕ, respectively, at 68% confidence level. The optimized R differs by 0.09 Å from our initial DFT result, and ϕ differs by 0.5°, which is within the error limits. When R and ϕ varies, the Br'-Br'' distance changes accordingly, as indicated by dashed lines in Figure 6g. As the long Br'-Br'' distance is present only in *iso*-$CHBr_2$-Br, we calculated its value while R and ϕ were optimized. The best fit value for Br'-Br'' distance is found to be 5.08 ±0.02 Å at the optimal R and ϕ. The optimal values and experimental errors (at 68% confidence limits) are given in Table 1.

5. EPR spectroscopy observations of photogenerated radicals

Electron paramagnetic resonance (EPR) spectroscopy was used to detect radical species generated from the photolysis of frozen bromoform solutions at low temperature, and follow their reactions. The first step was to identify the $CHBr_2$ radical, the tentative product of R1. We did not find any previous report on its magnetic parameters, although similar radicals have been reported.[18] Using DFT theory, we calculated hyperfine coupling (hfc) tensors for the proton and bromine nuclei in this radical. The latter exists as a set of three isotopomers (^{79}Br:^{79}Br, ^{79}Br:^{81}Br, and ^{81}Br:^{81}Br, with their relative abundances dictated by the natural abundances of the bromine isotopes, both of which have spin-3/2), as shown in Figure S15. We simulated these EPR spectra using hfc tensors calculated by DFT method and adjusted $\boldsymbol{g}$-tensor as described in the caption, in order to attribute the features of the experimental EPR spectra shown in Figure S16. The

characteristic features of these EPR spectra are a set of low-field lines 1 to 3 originating from the $CHBr_2$ radical with $\boldsymbol{B}||Z$ (where $\boldsymbol{B}$ is the magnetic field of the spectrometer), see Figure S15. As the hfc of deuteron (spin-1) is only 15% of that of proton (spin-1/2), the hyperfine splitting in $CDBr_2$ radical is negligible, whereas the proton splitting in $CHBr_2$ radical is significant (~24 G), therefore each resonance line becomes twinned, as shown in Figures S16 and S17.

Figure S16 shows the EPR spectrum obtained by 355 nm laser photolysis of 1 wt% $CDBr_3$ in frozen methylcyclohexane glass. Lines 2 and 3 indicated in Figure S15 are observed in this trace, yielding an estimate of $A_{cc}(^{79}Br)\approx 88$ G (vs. 80 G estimated by DFT), suggesting that this EPR spectrum indeed originates from $CDBr_2$. Our previous research indicates that the resonance lines from trapped Br atoms are extremely broad and cannot be observed in this field range,[19] therefore the spectral overlap is negligible.

Figure S17 shows the first-derivative EPR spectra of photoirradiated frozen solution of $CHBr_3$ in methanol-h_4. The most prominent feature is the triplet resonance lines from the CH_2OH radical (shadowed in the plot). Also, a doublet line from HCO radical and a set of resonance lines marked with open circles are observed. As light exposure prolonged, secondary photolysis of CH_2OH radicals occurred, resulting in an increase of HCO (Figure S18). Also, with longer exposure, when more $CHBr_2$ radicals are generated, the resonance lines indicated in Figure S18 become clear, suggesting that these lines are parts of the multiplet shown in Figure S15. In particular, there are well resolved, twinned lines 2 and 3 with $A_{bb}(^1H) \approx 23.5 \pm 0.5$ G (vs. 24.3 G estimated by DFT) and $A_{cc}(^{79}Br) \approx 88 \pm 2$ G, which corresponds to the $CDBr_2$ radical in methylcyclohexane (Figure S16). This clinches the identification of $CHBr_2$ in these solid matrices, providing direct evidence for R1.

By double integration of these EPR spectra, we found that the yield of $CHBr_2$ radical is approximately equal to that of CH_2OH radical. Since the H abstraction from the methanol by the $CHBr_2$ radical is endergonic (see Table S2), abstraction reaction R9 in Table S2 is unlikely to occur at 50 K. Rather, we believe (as was the case in other systems we recently studied)[19] that the excitation of $CHBr_3$ yields a "hot" Br atom that can directly abstract H atom from alcohols (while a thermalized Br atom can not):

$$CHBr_3 + h\nu \rightarrow CHBr_2 + Br^* \quad \text{(S2)}$$

$$Br^* + CH_3OH \rightarrow HBr + CH_2OH \quad \text{(S3)}$$

Reaction S3 competes with relaxation of the "hot" Br atom to a thermalized one. To further support this claim, we studied the photolysis of $CHBr_3$ in another alcohol, 2-propanol. The H atom abstraction from this alcohol yields 2-propyl radical, $(CH_3)_2COH$. In the EPR spectrum measured for 355 nm photolysis of $CHBr_3$ in 2-propanol, a multiplet arising from six equivalent protons of $(CH_3)_2COH$ is observed together with the resonance lines of the $CHBr_2$ radical (Figures S20 and S21). When 2-propanol-d_8, instead of 2-propanol-h_8, is used, the EPR spectrum of the 2-propyl-d_7 radical "collapses" to a single line, because the magnetic moment of deuteron is only 15% of the proton, and it is spin-1 nucleus rather than spin-1/2 nucleus, in the perdeutero isotopomer the septet of resonance lines from six equivalent methyl protons in 2-propan-olyl-h7 radical (separated by ca. 20 G) collapses to a closely spaced 15-let, which is not resolved in the EPR spectrum due to magnetic anisotropies, and so this multiplet collapses to a single, broad resonance line. As a result, one obtains an unobscured view of $CHBr_2$ radical. This experiment suggests that the concerted reactions are typical for all alcohols.

Figure S21 shows the evolution of EPR spectra from irradiated frozen 2-propanol-d_8 as the sample temperature increases. To facilitate comparison, we normalized these EPR spectra by $CHBr_2$ signal, as shown in the plot. As the temperature rises, the relative amplitude of the signal from 2-propyl-d_7 radical decreases and disappears completely at 125 K (with only $CHBr_2$ remains), which is well below the softening point of 2-propanol glass. This is the classical signature of a thermally activated reaction: the 2-propyl-d_7 radical selectively decays, while the $CHBr_2$ radical remains in the matrix. This suggests that the 2-propyl-d_7 radical reacts with $CHBr_3$ by abstracting a Br atom (which is fully analogous to reaction R14 in Table S2 for methanol)

$$(CD_3)_2COD + CHBr_3 \rightarrow (CD_3)_2CBrOD + CHBr_2 \qquad (S4)$$

We conclude that (i) a "hot" Br atom generated in the photolysis of bromoform can abstract a H from the solvent and (ii) the resulting H loss solvent radical can abstract a Br atom from a $CHBr_3$ molecule, yielding another $CHBr_2$ radical. Combining reactions R9 and R14 (Table S2) for methanol, we obtain the cycle illustrated in Figure S22. The reaction product ($BrCH_2OH$) subsequently decomposes into HBr and H_2CO, which is similar to chloromethanol, which is known to decompose to HCl and formaldehyde, (reaction R17 in Table S2).[20] Note that the same product

is formed in cross recombination of Br atoms and CH_2OH radicals (reaction R8 in Table S2). Importantly, while EPR can indicate the occurrence of radical reactions, it brings no information on their reaction rates.

6. Product analysis

Proton nuclear magnetic resonance (NMR) and gas chromatography mass spectrometry (GCMS) were used to analyze bromoalkane products generated by laser photolysis of $CHBr_3$ in liquid methanol and methylcyclohexane (see Supplementary Methods). Due to interference from impurity in the solvent, a relatively high concentration of the bromoform (50 mM) was used for accurate quantification of photoproducts. By using different NMR solvents (in which the chemical shifts of the photoproducts change significantly, as shown in Table S4 and Figures S23 to 25) to avoid the spectral overlap, we were able to identify the photoproducts quantitatively. These results are given in Table S3. The same photoreaction products were also identified with GCMS (Figure S26). The identities of photoproducts were established by mass spectra (including the signatures of bromine isotopes) and further verified by their retention times on the column through comparisons with reference compounds. Using appropriate calibration mixtures, the reaction yields were quantified (Table S3) and found to be in good agreement with the values obtained from NMR measurements. As seen from Figure S27, when $CHBr_3$ is photolyzed in CD_3OD, $CHDBr_2$ was formed instead of CH_2Br_2. This suggests that dibromomethane is generated by H/D abstraction from methanol (cf. reaction R9 in Table S2).

$$CHBr_2 + CD_3OD \rightarrow CHDBr_2 + CD_2OD. \qquad (S5)$$

In addition, three other products identified by GCMS and NMR are 1,1,2,2-tetrabromoethane ($C_2H_2Br_4$) and *cis*- and *trans*-isomers of the 1,2-dibromoethylene ($C_2H_2Br_2$) generated via reactions R11 and R12 in Table S2. The preponderance (~2:1) of *cis* isomer over *trans* isomer is typical for radical disproportionation. These products were the same in the protiated and deuterated methanol.

With the insights brought by the above analysis, most of radical reactions shown in Table S2 have been established. Reactions R1 and R2 are well known. Reaction R16 is well known in the radiation chemistry and photochemistry of the methanol. Reactions R15 is analogous to many other such reactions involving alkyl radicals and molecular bromine. Radical reactions R1 to R16 form the complete set; it is *the minimal such set that involves all of the experimentally observed radicals and the products of their reactions.*

We calculated the standard heats of these reactions using DFT methods (Table S2). It can be seen that most of these reactions are strongly exothermic (~100 kJ mol^{-1}), and we can assume that such reactions are diffusion-controlled (keep in mind that the Br atom is much more diffusive than all other radicals in this photosystem).

7. Supplementary Methods

Product analysis. For product analysis, we used the same laser setup at 267 nm that was used in our TRXL experiments. 5 mL of deaerated methanol solution of $CHBr_3$ (50 mM) was irradiated for 1 h in a sealed Suprasil optical cuvette with an optical path of 10 mm. During the photolysis, the solution was vigorously stirred using a magnetic bar.

Nuclear Magnetic Resonance (NMR). NMR spectra were measured using an Avance DMX 500 MHz spectrometer (Bruker) and the chemical shifts were calculated *vs*. tetramethylsilane. Photolyzed methanol-d_4 solutions were analyzed without further treatment; methanol-h_4 solutions were first diluted 1:10 v/v with a deuterated solvent (methanol-d_4, chloroform-*d*, and dimethylsulfoxide-d_6, Table S4) and the presaturation (*zpgr* sequence) was used to suppress CH_3OH resonances. Chemical shifts of brominated photoproducts vary in different solvents (see Table S4). As their resonance lines overlap with impurities and solvent, two to three solvents were used for unambiguous determination. To this end, NMR lines were integrated and referenced to $CHBr_3$ (Table S3). As there is only one kind of protons in these products, their NMR spectra are singlet lines. To identify these products, SDBS NMR database from AIST was used.[21] The candidate species were then purchased from Aldrich to generate Table S3 and used for GCMS calibrations (see below).

Gas Chromatography – Mass Spectrometry (GCMS). For GCMS analysis, 1 µL liquid sample was loaded on an HP-5MS (0.25 µm, 30 m) column using an Agilent Technologies Model 7890B chromatograph equipped with a Model 5977 mass detector. For chromatographic analysis, the temperature was first maintained at 35 ^{o}C for 6 minutes, then increased to 250 ^{o}C at the rate of 20 ^{o}C/min and held for another 5 minutes. The typical chromatogram (the total ion current vs. the retention time on the capillary column) is shown in Figures S26a and S26b (note the logarithmic scale of the vertical axis). Brominated products are readily recognized through their isotope multiplets (originating from ^{79}Br and ^{81}Br, see EPR section). The identification of photoproducts by mass spectrometry was then confirmed by checking the retention time relative to reference compounds. The product yields were quantified through integration of the total ion current. Prepared mixtures of $CHBr_3$, CH_2Br_2, $C_2H_2Br_2$, and $C_2H_2Br_4$ were used for calibration.

Matrix isolation Electron Paramagnetic Resonance (EPR) spectroscopy. Liquid samples containing 1-10 wt% $CXBr_3$ (X=H,D) were placed in 4 mm diameter Suprasil tubes and degassed in vacuum through repeated freeze-thaw cycles. The tubes were flame sealed and immersed in liquid nitrogen. The samples were then placed in an optical dewar and irradiated at 77 K using 355 nm laser pulses (35 mJ, 6 ns fwhm) from a Nd:YAG laser (Quantel Brilliant) operating at 10 Hz. In some measurements, water-filtered output of 60 W Xe arc lamp was used instead. Photogenerated radicals were measured in this matrix using a 9.44 GHz Bruker ESP300E spectrometer, with the sample placed in a flow ^{4}He cryostat (Oxford Instruments CF935). The magnetic field $\boldsymbol{B}$ and the hyperfine coupling (hfc) constants of these radicals are given in the units of Gauss (1 G = 10^{-4} T). If not stated otherwise, the first derivative EPR spectra were obtained using 2 mW of microwave power and 10 G modulation at 100 kHz at 50 K. The hfc constants (hfcc's) and radical structures were calculated using B3LYP functional and 6-31+G(d,p) basis set from Gaussian 09 (see the Methods). The principal axes of $\boldsymbol{A}$- (hyperfine) and $\boldsymbol{g}$-tensors are labelled as (a, b, c) and (X,Y,Z) respectively. The powder EPR spectra were simulated using second-order perturbation theory assuming arrested rotation of the radicals in a low temperature solid matrix.

8. Supplementary references

1. J. H. Lee, J. Kim, M. Cammarata, Q. Y. Kong, K. H. Kim, J. Choi, T. K. Kim, M. Wulff and H. Ihee, *Angew. Chem. Int. Ed.* 2008, **47,** 1047.

2. Q. Y. Kong, M. Wulff, J. H. Lee, S. Bratos and H. Ihee, *J. Am. Chem. Soc.* 2007, **129,** 13584.

3. H. Ihee, M. Lorenc, T. K. Kim, Q. Y. Kong, M. Cammarata, J. H. Lee, S. Bratos and M. Wulff, *Science* 2005, **309,** 1223.

4. K. S. Kjær, T. B. van Driel, J. Kehres, K. Haldrup, D. Khakhulin, K. Bechgaard, M. Cammarata, M. Wulff, T. J. Sørensen, and M. M. Nielsen, *Phys. Chem. Chem. Phys.* 2013, **15,** 15003.

5. L. X. Chen, W. J. H. Jäger, G. Jennings, D. J. Gosztola, A. Munkholm and J. P. Hessler, *Science* 2001, **292,** 262.

6. L. X. Chen and X. Y. Zhang, *J. Phys. Chem. Lett.* 2013, **4,** 4000.

7. X. Y. Zhang, S. E. Canton, G. Smolentsev, C. Wallentin, Y. Z. Liu, Q. Y. Kong, K. Attenkofer, A. B. Stickrath, M. W. Mara, L. X. Chen, K. Wärnmark and V. Sundström, *J. Am. Chem. Soc.* 2014, **136,** 8804.

8. M. J. Frisch, G. W. Trucks, H. B. Schlegel, G. E. Scuseria, M. A. Robb, J. R. Cheeseman, G. Scalmani, V. Barone, B. Mennucci, G. A. Petersson, H. Nakatsuji, M. Caricato, X. Li, H. P. Hratchian, A. F. Izmaylov, J. Bloino, G. Zheng, J. L. Sonnenberg, M. Hada, M. Ehara, K. Toyota, R. Fukuda, J. Hasegawa, M. Ishida, T. Nakajima, Y. Honda, O. Kitao, H. Nakai, T. Vreven, J. A. Montgomery, Jr., J. E. Peralta, F. Ogliaro, M. Bearpark, J. J. Heyd, E. Brothers, K. N. Kudin, V. N. Staroverov, R. Kobayashi, J. Normand, K. Raghavachari, A. Rendell, J. C. Burant, S. S. Iyengar, J. Tomasi, M. Cossi, N. Rega, J. M. Millam, M. Klene, J. E. Knox, J. B. Cross, V. Bakken, C. Adamo, J. Jaramillo, R. Gomperts, R. E. Stratmann, O. Yazyev, A. J. Austin, R. Cammi, C. Pomelli, J. W. Ochterski, R. L. Martin, K. Morokuma, V. G. Zakrzewski, G. A. Voth, P. Salvador, J. J.

Dannenberg, S. Dapprich, A. D. Daniels, O. Farkas, J. B. Foresman, J. V. Ortiz, J. Cioslowski, D. J. Fox, *Gaussian 09, Revision A.1*, Gaussian, Inc., Wallingford CT, 2009.

9. A. D. Becke, *J. Chem. Phys.*1993, **98,** 5648.

10. C. Lee, W. Yang and R. G. Parr, *Phys. Rev. B* 1988, **37,** 785.

11. J. P. Perdew and Y. Wang, *Phys. Rev. B*, 1992, **45,** 13244.

12. J. P. Perdew, K. Burke and M. Ernzerhof, *Phys. Rev. Lett.* 1996, **77,** 3865.

13. J. P. Perdew, K. Burke and Y. Wang, *Phys. Rev. B,* 1996, **54,** 16533.

14. A. D. Mclean and G. S. Chandler, *J. Chem. Phys.* 1980, **72,** 5639.

15. V. Barone and M. Cossi, *J. Phys. Chem. A* 1998, **102,** 1995.

16. F. Neese, *WIRE Comput. Mol. Sci.* 2012, **2,** 73.

17. P. R. Bevington and D. K. Robinson, 2003, McGraw Hill, New York, NY.

18. P. N. Bajaj, and R. M. Iyer, *Radiat. Phys. Chem.* 1980, **16,** 21.

19. I. A. Shkrob, T. W. Marin, R. A. Crowell and J. F. Wishart, *J. Phys. Chem. A* 2003, **117,** .5742.

20. D. L. Phillips, C. Zhao, and D. A. Wang, *J. Phys. Chem. A* 2005, **109,** 9653.

21. T. Yamaji, T. Saito, K. Hayamizu, M. Yanagisawa and O. Yamamoto, O. SDBS; *National Institute of Advanced Industrial Science and Technology*, 2016.

Supporting tables

Table S1. Relative energies (kJ mol-1) of candidate reaction intermediates in methanol and methylcyclohexane (in parentheses), obtained using B3LYP/6-311++G(3df,3pd) method and the CPCM solvent model. The photon energy at 267 nm is 448.4 kJ mol-1. The channels are arranged in the order of the increasing reaction energy.

Species	Relative energies (kJ mol^{-1})
$CHBr_3$	0.0 (0.0)
iso-$CHBr_2$-Br	130.2 (165.7)
HBr + CBr_2	206.0 (243.6)
$CHBr_2$ + Br	229.1 (237.5)
CHBr + Br_2	315.4 (333.9)
CBr_3 + H	380.1
HBr + CBr + Br	459.3 (504.3)
CHBr + 2Br	514.9 (537.8)
CH + Br_2 + Br	640.1 (671.9)
CH + 3Br	839.7 (875.8)

Table S2. Calculated enthalpies (kJ mol-1) for candidate reaction channels initiated by photoexcitation of $CHBr_3$ in methanol and methylcyclohexane (in parentheses). These energetics were calculated using B3LYP/6-311++G(3df,3pd) method and the CPCM solvent model.

	Reactions	Energies (kJ mol^{-1})
R1	$CHBr_3 \rightarrow CHBr_2 + Br$	229.1 (237.5)
R2	$CHBr_3 \rightarrow$ *iso*-$CHBr_2$-Br	130.2 (165.7)
R3	*iso*-$CHBr_2$-Br + $CH_3OH \rightarrow CH_3OCHBr_2$ + HBr	-166.48
R4	$CHBr_2 + Br \rightarrow CHBr_3$	-229.1 (-237.5)
R5	$2\ Br \rightarrow Br_2$	-201.38 (-203.94)
R6	$CHBr_2 + Br \rightarrow$ iso-$CHBr$-$_2$-Br	98.9 (71.8)
R7	*iso*-$CHBr_2$-Br $\rightarrow CHBr_3$	-130.2 (-165.7)
R8	$Br + CH_2OH \rightarrow BrCH_2OH$	-288.07
R9	$CHBr_2 + CH_3OH \rightarrow CH_2Br_2 + CH_2OH$	6.77
R10	$CHBr_2 + Br_2 \rightarrow CHBr_3 + Br$	36.38 (33.51)
R11	$2\ CHBr_2 \rightarrow C_2H_2Br_4$	-294.63 (-300.01)
R12	$2\ CHBr_2 \rightarrow C_2H_2Br_2 + Br_2$	-245.47(-250.54)

R13	$CHBr_2 + CH_2OH \rightarrow CH_2Br_2 + H_2CO$	-272.47
R14	$CH_2OH + CHBr_3 \rightarrow BrCH_2OH + CHBr_2$	-50.31
R15	$CH_2OH + Br_2 \rightarrow BrCH_2OH + Br$	-86.69
R16	$2\ CH_2OH \rightarrow CH_3OH + H_2CO$	-115.78
R17	$BrCH_2OH \rightarrow HBr + H_2CO$	41.06
R18	$CHBr_2 + Br \rightarrow$ *iso*-$CHBr_2$-Br	-103.03 (-71.74)
R19	$Br + CH_3OH \rightarrow HBr + CH_2OH$	32.23
R20	$CHBr_2 + CH_3OH \rightarrow CH_3OCHBr_2 + H$	130.43
R21	$HBr + CH_3OH \rightarrow CH_3Br + H_2O$	-33.84
R22	$CHBr_2 + C_7H_{14} \rightarrow CH_2Br_2 + C_7H_{13}$	(-9.47)

Table S3. Product yields in 267 nm laser photolysis of 50 mM $CHBr_3$ in CH_3OH as determined by ^1H NMR and GCMS.

	mole ratio, % (relative to $CHBr_3$)			
photoproduct	NMR $CDCl_3$	NMR CD_3OD	NMR $(CD_3)_2SO$	GCMS
CH_2Br_2	4.4	-	5.1	3.2
$Br_2CHCHBr_2$	3.3	4.0	4.7	4.2
cis-BrCH=CHBr [a]	4.8	4.9	4.4	3.9
trans-BrCH=CHBr [a]	1.8	2.0	2.6	1.8

a) The relative yields of cis- and trans- isomers of 1,2-dibromoethylene determined using ^{13}C NMR is 2.2:1.

Table S4. Chemical shifts (in parts per million vs. tetramethylsilane) for bromoalkane photoproducts in different NMR solvents.

photoproducts	$CDCl_3$			CD_3OD		$(CD_3)_2SO$
	d(^{1}H)	d(^{1}H)	d(^{13}C)	d(^{1}H)	d(^{13}C)	d(^{1}H)
$CHBr_3$	6.827	6.88	9.74	7.4	11.03	7.66
CH_2Br_2	4.947	4.92	19.2	5.14	18.42	5.38
$Br_2CHCHBr_2$	6.04	6.04	46.91	6.53	-	6.89
cis-BrCH=CHBr	7.007	7.00	113.34	7.19	112.47	7.44
trans-BrCH=CHBr	6.625	6.62	107.11	6.85	106.42	7.09

Table S5. Optimal model parameters from the combined global fitting analysis of the TRXL and XTA data in both solvents. The ratios of the initial concentrations of Br ($CHBr_2$) and isomer are forced to be equal in the TRXL and XTA fits. Uncertainties are estimated as the highest confidence boundary for χ^2_{comb} to deviate by 0.1% from the optimal value.

Solvent	χ^2_{comb}	k_{R4} [$M^{-1}\cdot s^{-1}$]	k_{R5} [$M^{-1}\cdot s^{-1}$]	$k_{R3/R7}$ [$M^{-1}\cdot s^{-1}$]	k_{R6} [$M^{-1}\cdot s^{-1}$]	F_{fast}	ΔE_{XAS} [eV]
CH_3OH	1.0376	$0 \pm 2.6\cdot10^8$	$(7.31 \pm 1.0)\cdot10^9$	$(9.8 \pm 0.8)\cdot10^9$	-	0.184 ± 0.003	-0.411 ± 0.014
C_7H_{14}	1.1294	$0 \pm 2\cdot10^6$	$(5.04 \pm 0.7)\cdot10^8$	$(7.7 \pm 1.6)\cdot10^6$	$0 \pm 2\cdot10^6$	0.0383 ± 0.0003	0.51 ± 0.03

Supporting Figures

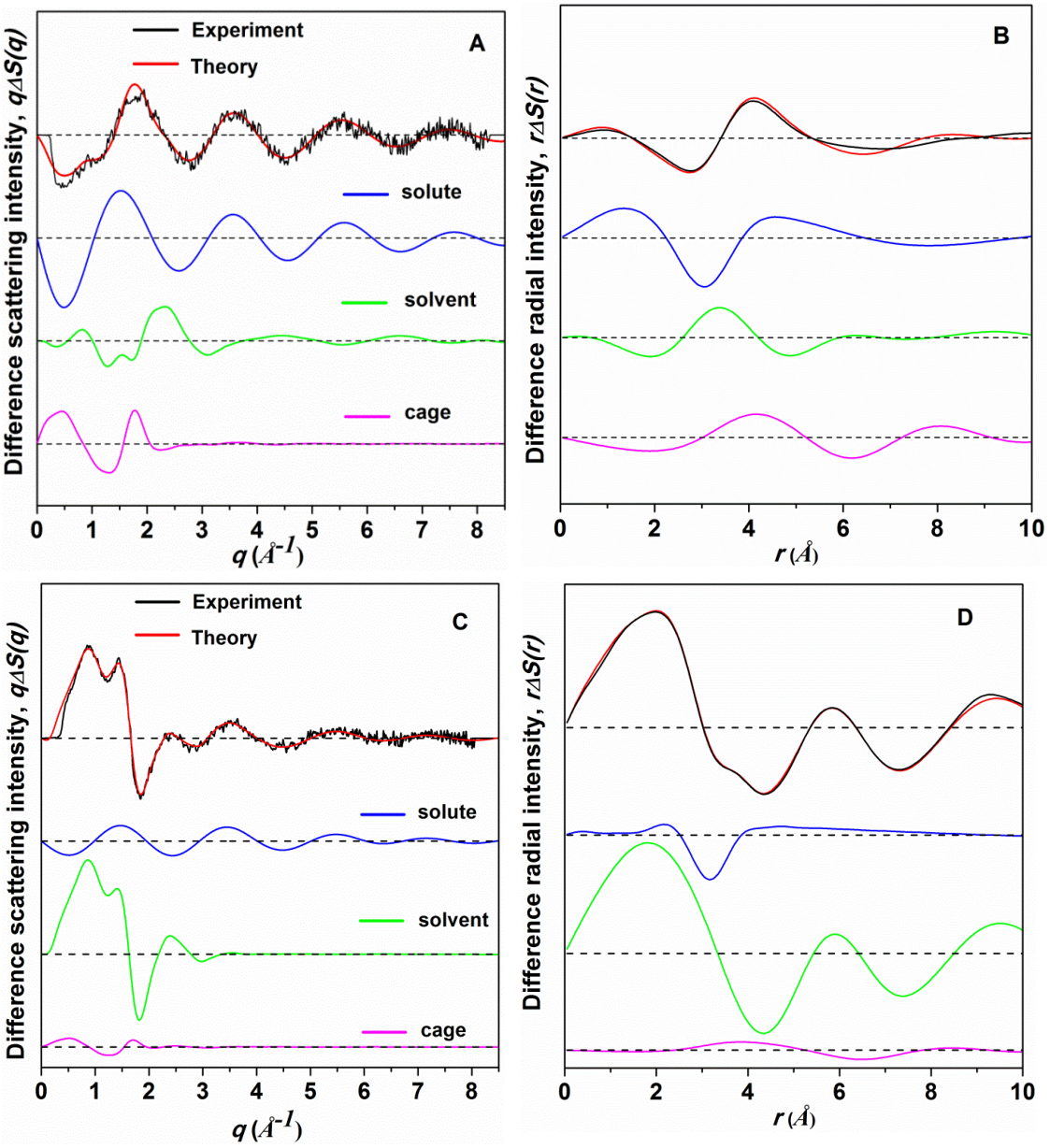

Figure S1. TRXL traces for laser photolysis of $CHBr_3$ in methanol. The experimental difference scattering curves (*in black*) were obtained at (**a,b**) 100 ps and (**c,d**) 1 µs. The simulated traces (*in red*) include three contributions: solute term (*blue*), solvent term (*green*), and solute/solvent cage term (*magenta*). Difference radial intensity $r\Delta S(r)$ in panels b and d are sine-Fourier transforms of $q\Delta S(q)$ traces shown in panels a and c. The prominent negative peak at 3.25 Å (corresponding to Br···Br distance in the bromoform) in panel b is due to depletion of $CHBr_3$ by light. The solvent signal dominates at 1 µs.

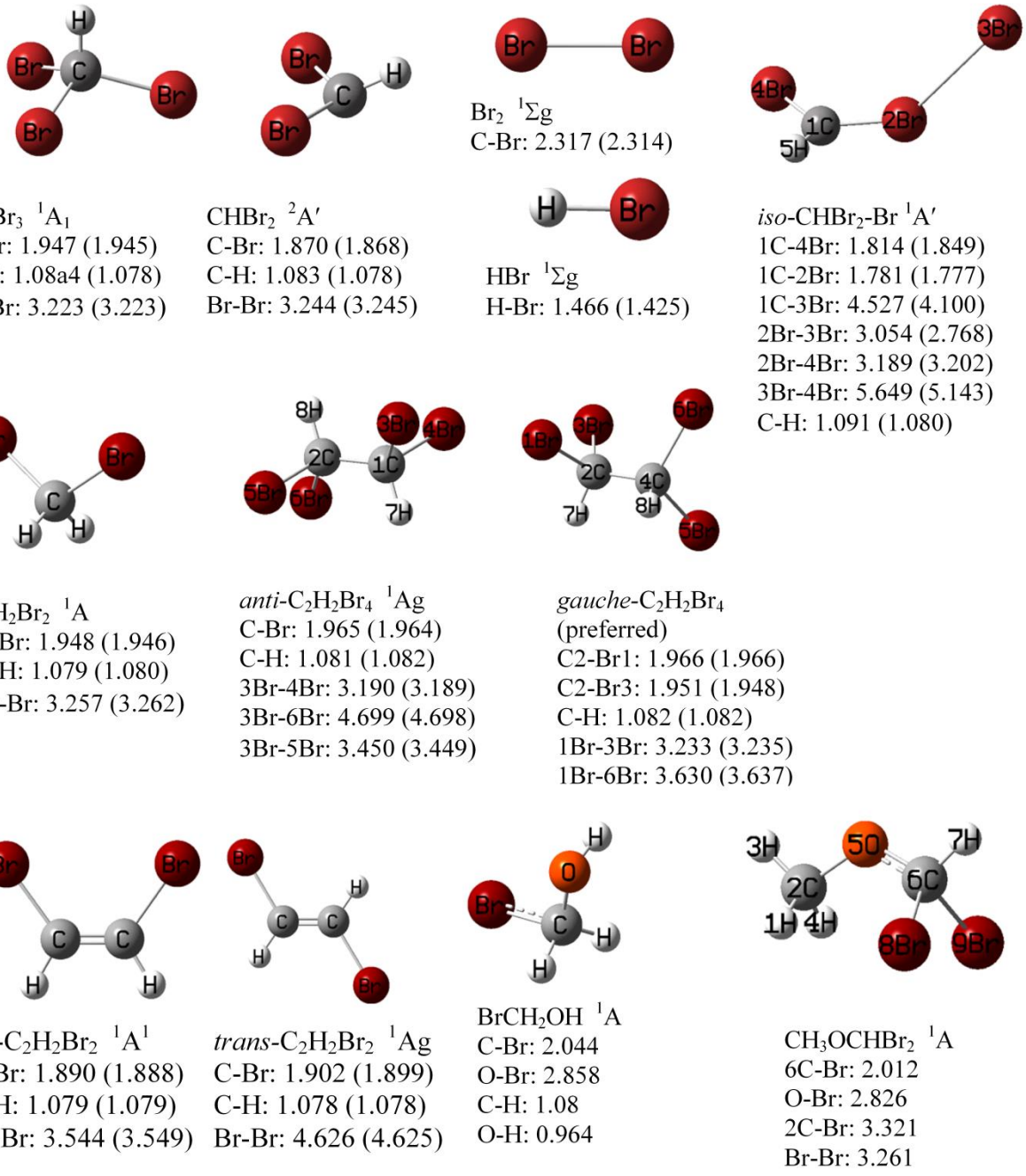

Figure S2. Optimized geometries and bond lengths (Å) of candidate intermediates involved in the photodissociation of $CHBr_3$ in methanol and methylcyclohexane (in parentheses). The B3LYP/6-311++G(3df,3pd) functional and the CPCM solvent model were used for the calculations.

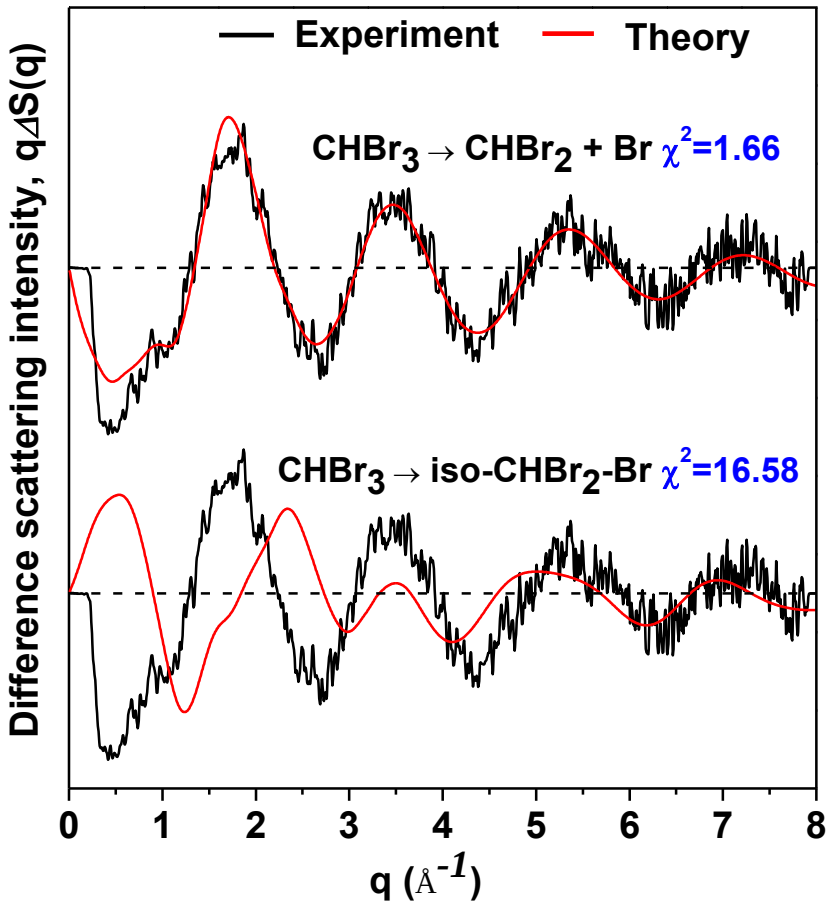

Figure S3. Analysis of the difference scattering intensity at 100 ps for $CHBr_3$ in methanol, assuming that this signal originates wholly through reaction R1 (*top*) or reaction R2 (*bottom*). The latter possibility is incompatible with our results. The figures of merit (χ^2) are indicated in the plot. When reactions R1 and R2 are simultaneously considered in the analysis, the contribution of reaction R2 converges to zero.

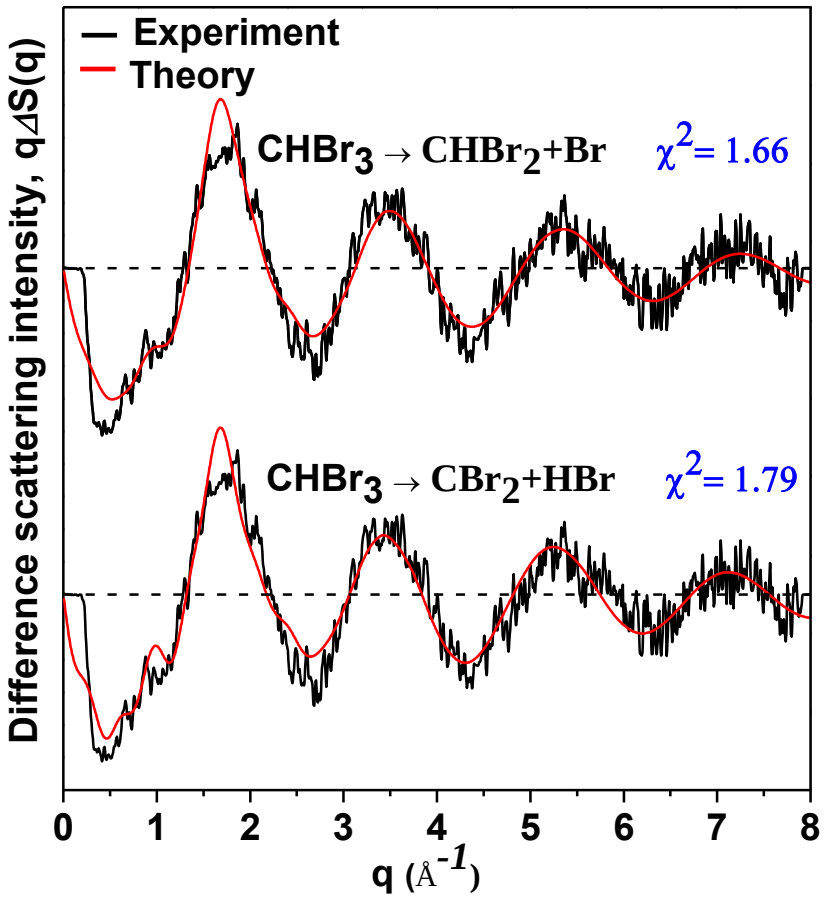

Figure S4. TRXL data for laser photolysis of $CHBr_3$ in methanol at 100ps. The experimental difference curve (black) is compared to two reaction channels as indicated in the plot. The upper reaction channel gives only a slightly better agreement. The figures of merit χ^2 are given in the plot.

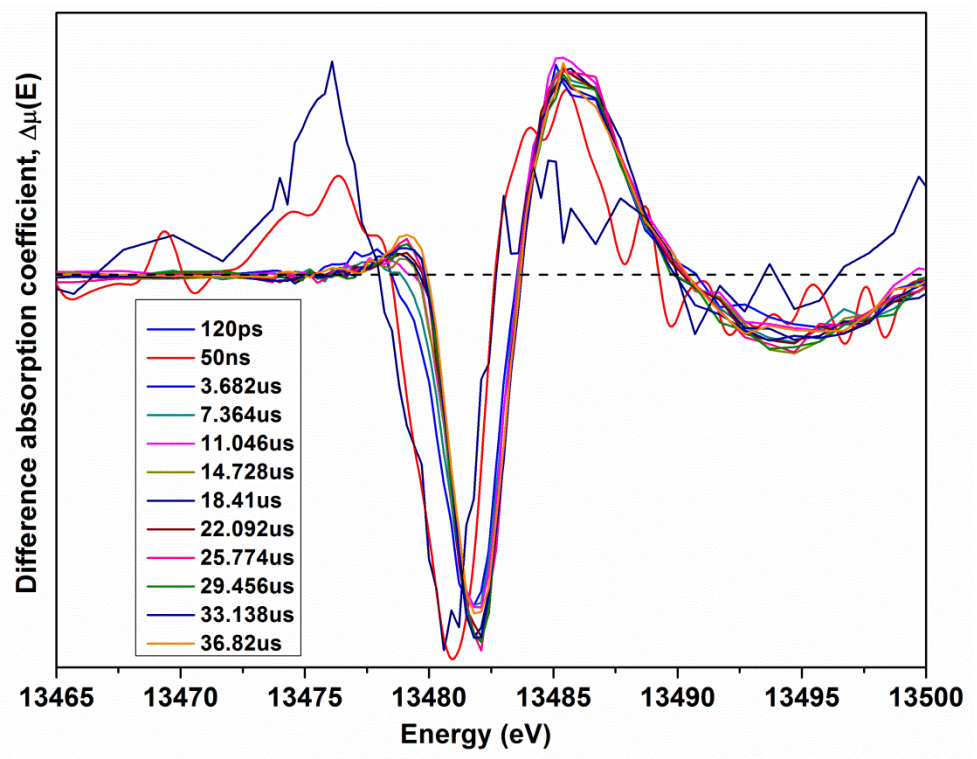

Figure S5. Difference X-ray absorption coefficients, $\Delta\mu$(E), for the photodissociation of $CHBr_3$ in methanol at selected delay times. These raw XTA spectra were obtained by subtracting the reference XAS spectrum (before laser excitation) from XAS spectra after the laser excitation. The concentration of $CHBr_3$ in methanol is 2mM.

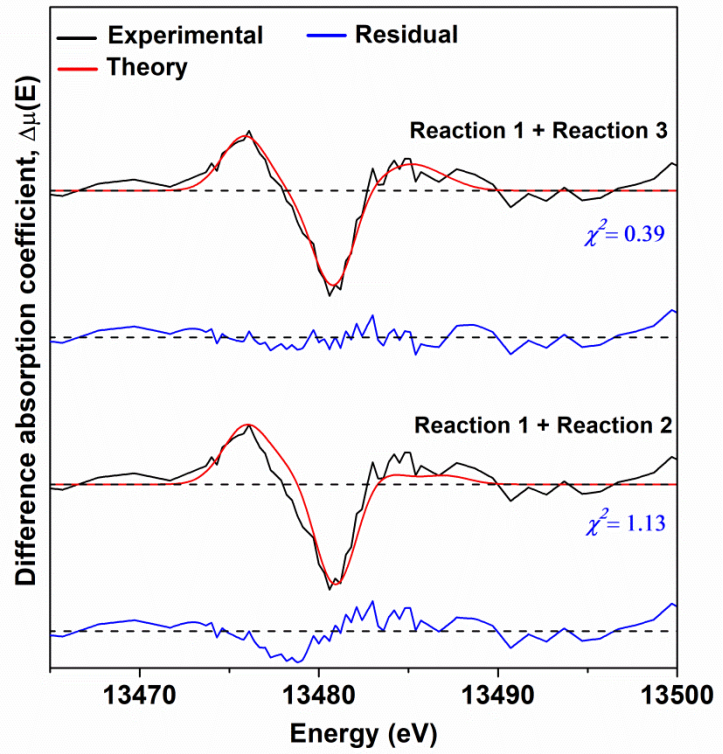

Figure S6. Fitting analysis of the XTA spectrum obtained 120 ps after laser photoexcitation of $CHBr_3$ in methanol with the theoretical spectra calculated for two reaction pathways. The experimental spectrum (black) is compared with simulated spectra (red) of two reaction channels: R1 and R3 (*top*) and R1 and R2 (*bottom*). The residuals (blue) between the experimental and theoretical spectra are also shown. It can be seen that the formation of isobromoform is not supported by our data. Its concentration converges to zero when two reaction channels are included simultaneously in the data analysis.

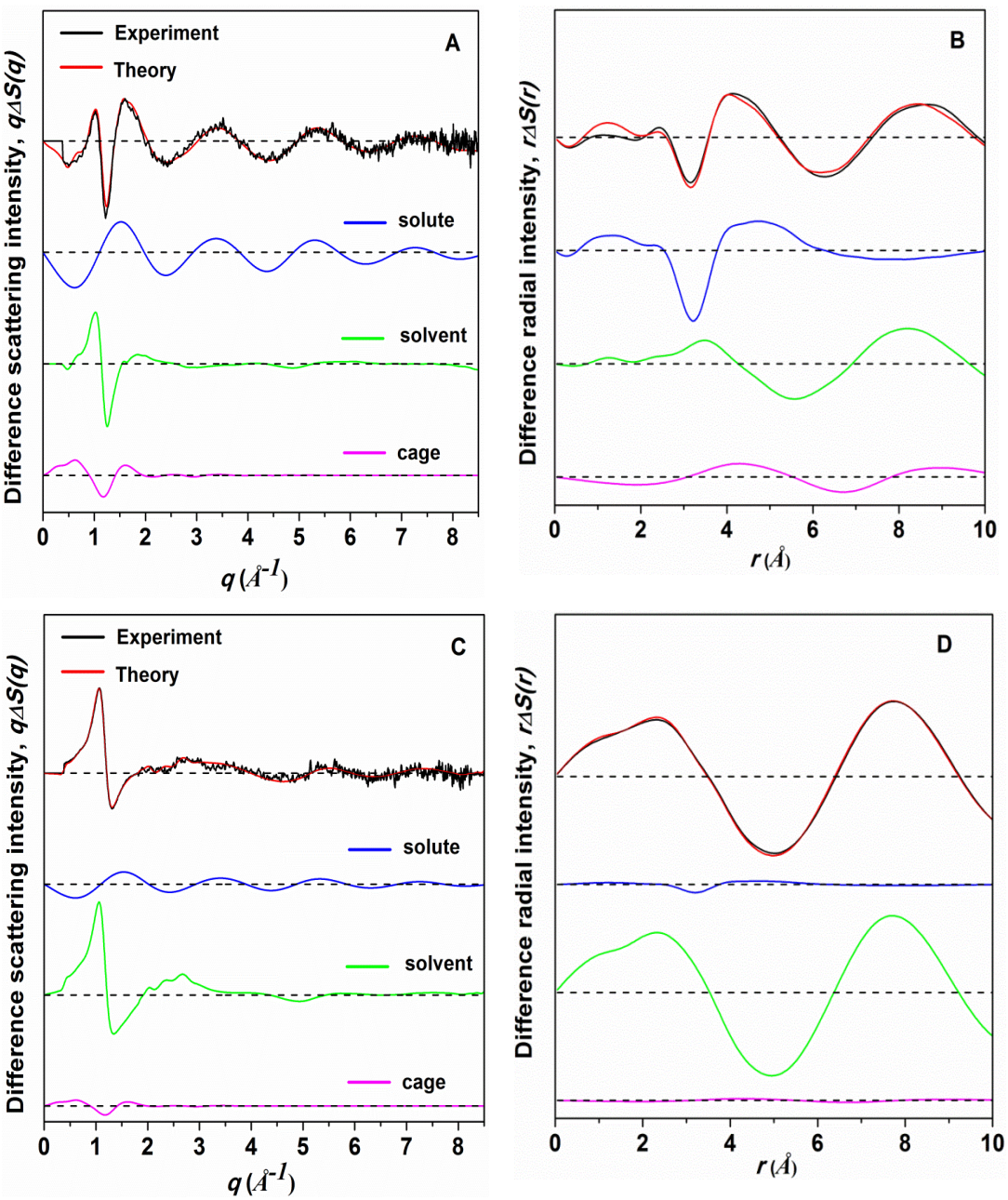

Figure S7. TRXL traces for laser photolysis of $CHBr_3$ in methylcyclohexane at 100 ps (a,b) and 1 μs (c,d). Data analysis is similar to Figure S1.

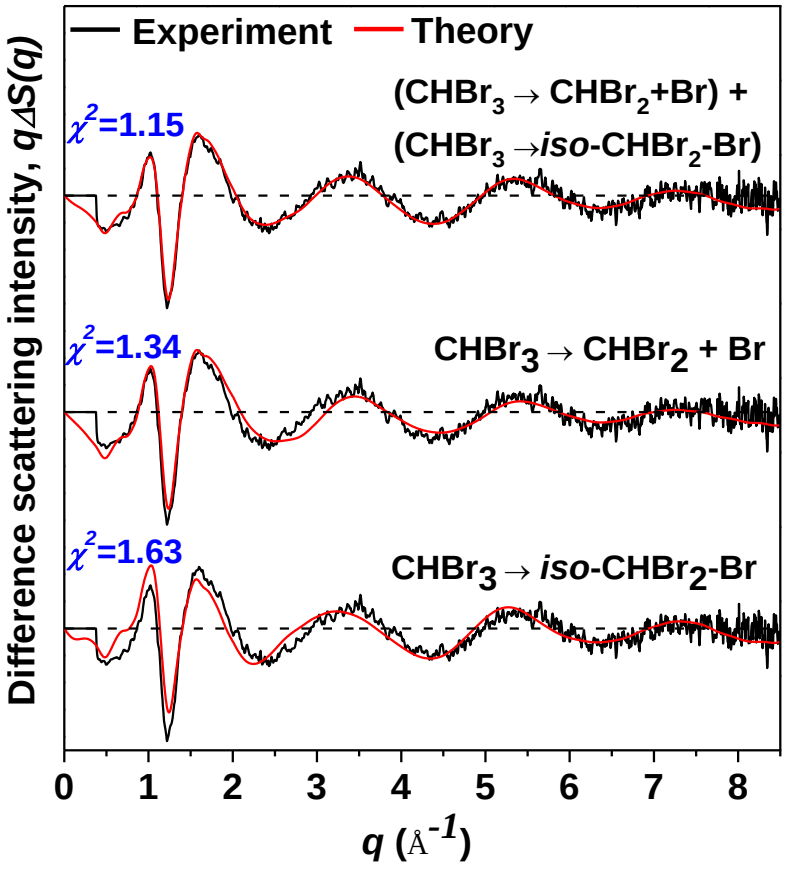

Figure S8. Analysis of TRXL data for $CHBr_3$ in methylcyclohexane. Both reactions R1 and R2 are needed to produce a good agreement with the experimental data at 100 ps. The figures of merit χ^2 are given in the plots.

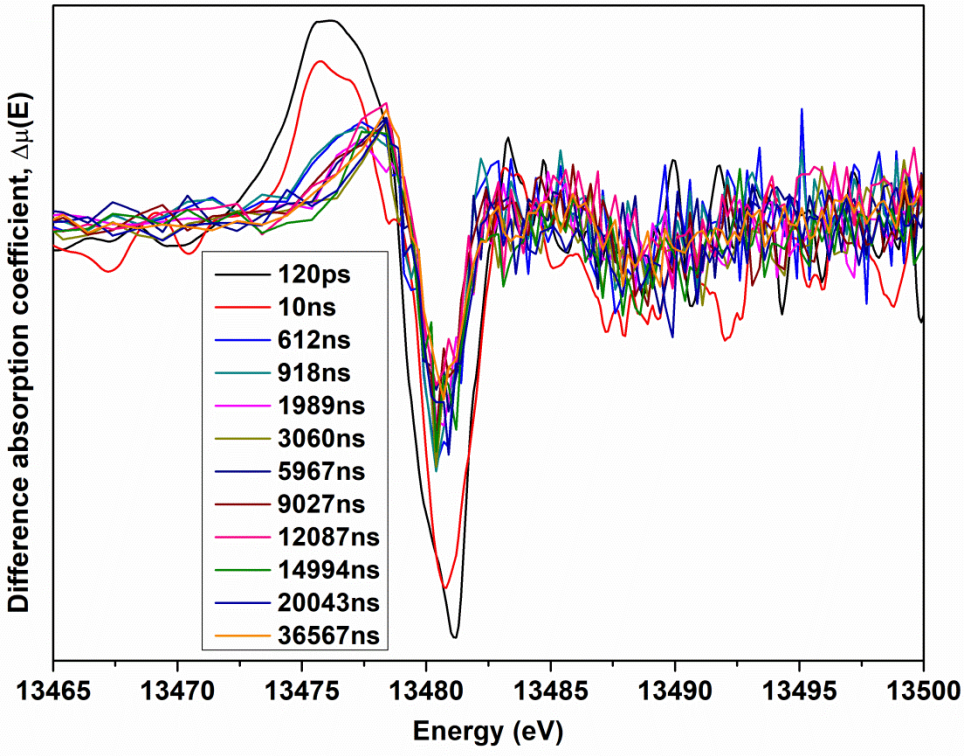

Figure S9. Difference absorption coefficient, $\Delta\mu$(E), for laser photoexcitation of 2 mM $CHBr_3$ in methylcyclohexane at selected delay times. These XTA spectra were obtained by subtracting the reference spectrum before laser excitation from XAS spectra measured after laser excitation.

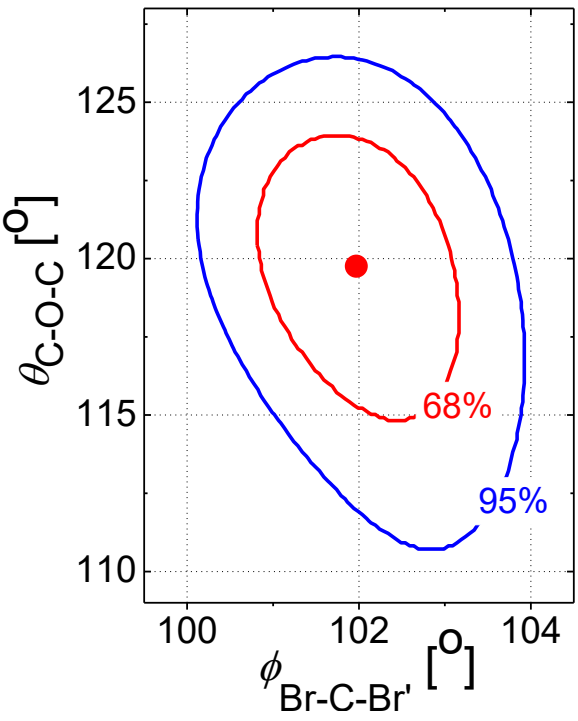

Figure S10. The figure of merit (χ^2) contour plots for CH_3OCHBr_2 structural fit. Shown in the plot is the projection of the χ^2 surface on the (ϕ,θ) plane. The red and blue ellipses represent statistical confidence areas of 68% and 95%, respectively. The red dot represents the optimal values of the structural parameters.

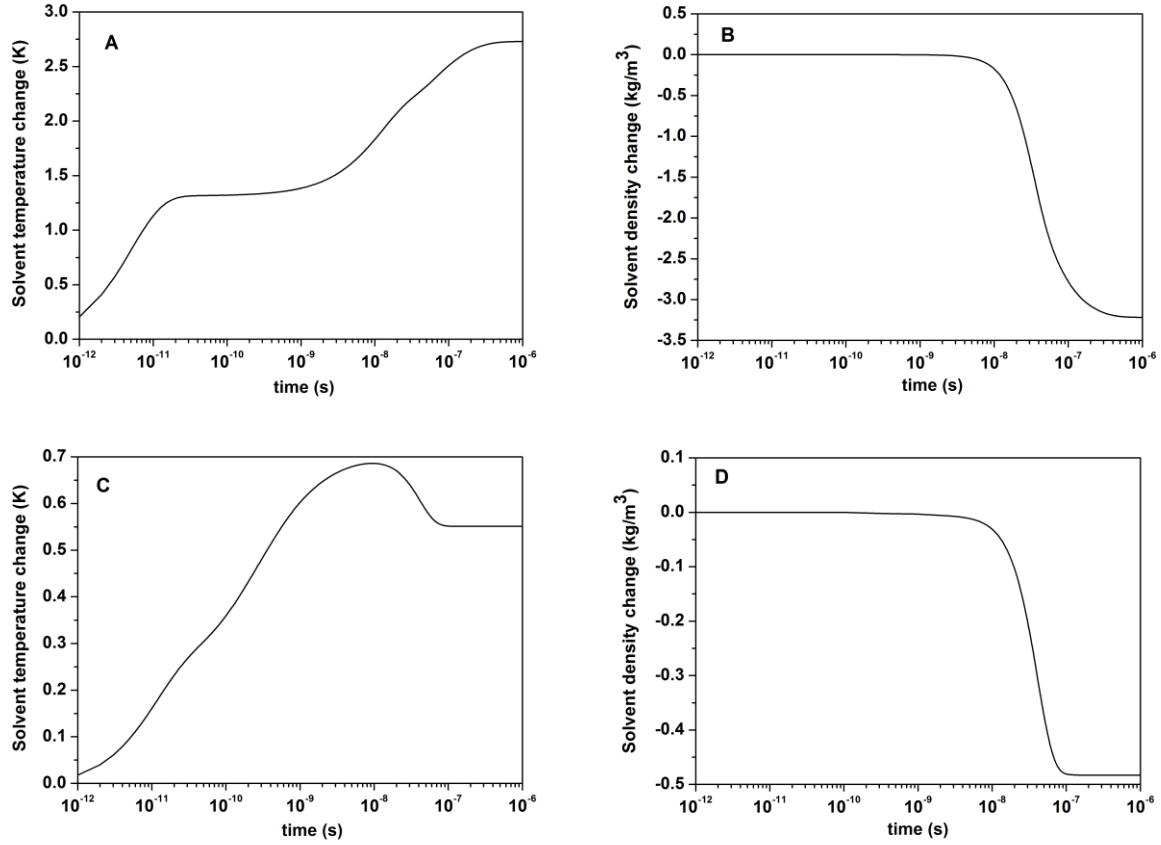

Figure S11. Time-dependent solvent temperature (panels A and C) and density (panels B and D) changes. Top: methanol; Bottom: methylcyclohexane.

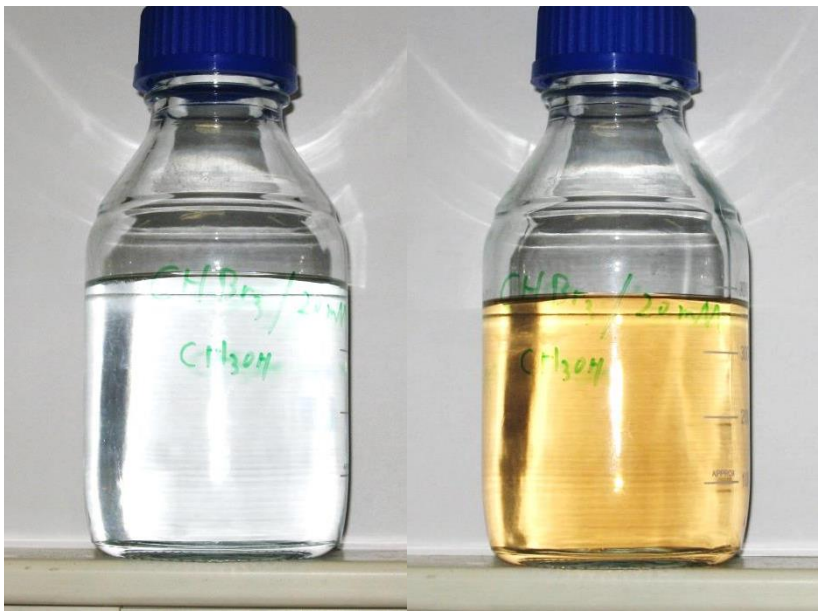

Figure S12. Molecular bromine generation in laser photolysis of $CHBr_3$ in methanol (color photograph). The $CHBr_3$ solution in methanol before (left) and after (right) 2 h photolysis at 267 nm.

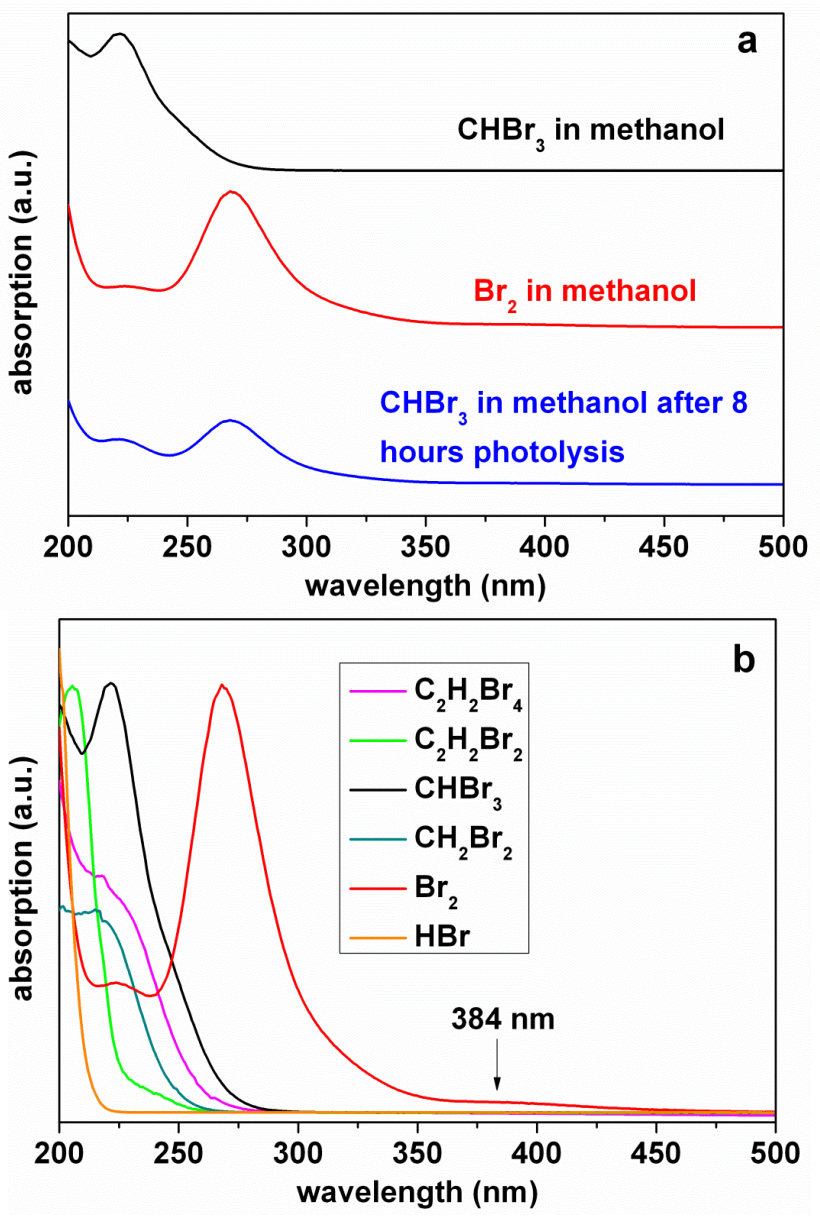

Figure S13. Spectrophotometry of photolyzed $CHBr_3$ in methanol after 257 nm laser irradiation. (a) the absorption spectra of $CHBr_3$ (black), fresh Br_2 (red) and $CHBr_3$ photolyzed by 257 nm for 8 hours (blue) in methanol, the concentrations of Br_2 and $CHBr_3$ are 5 mM. (b) the absorption spectra of $CHBr_3$ (black), Br_2 (red), $C_2H_2Br_4$ (magenta), $C_2H_2Br_2$ (green), CH_2Br_2 (cyan) and HBr (yellow) in methanol. Br_2 in methanol has strong absorption at 267 nm, which overlaps with the spectrum of $CHBr_3$ after 8 hours photolysis, and the weak absorption at 384 nm explains the orange color of the solution as shown in Figure S12, while the other species absorb below 280 nm and highly overlapped with $CHBr_3$, which have no contributions to the orange color of the solution. This comparison confirms Br_2 is formed by photolysis of $CHBr_3$ in methanol.

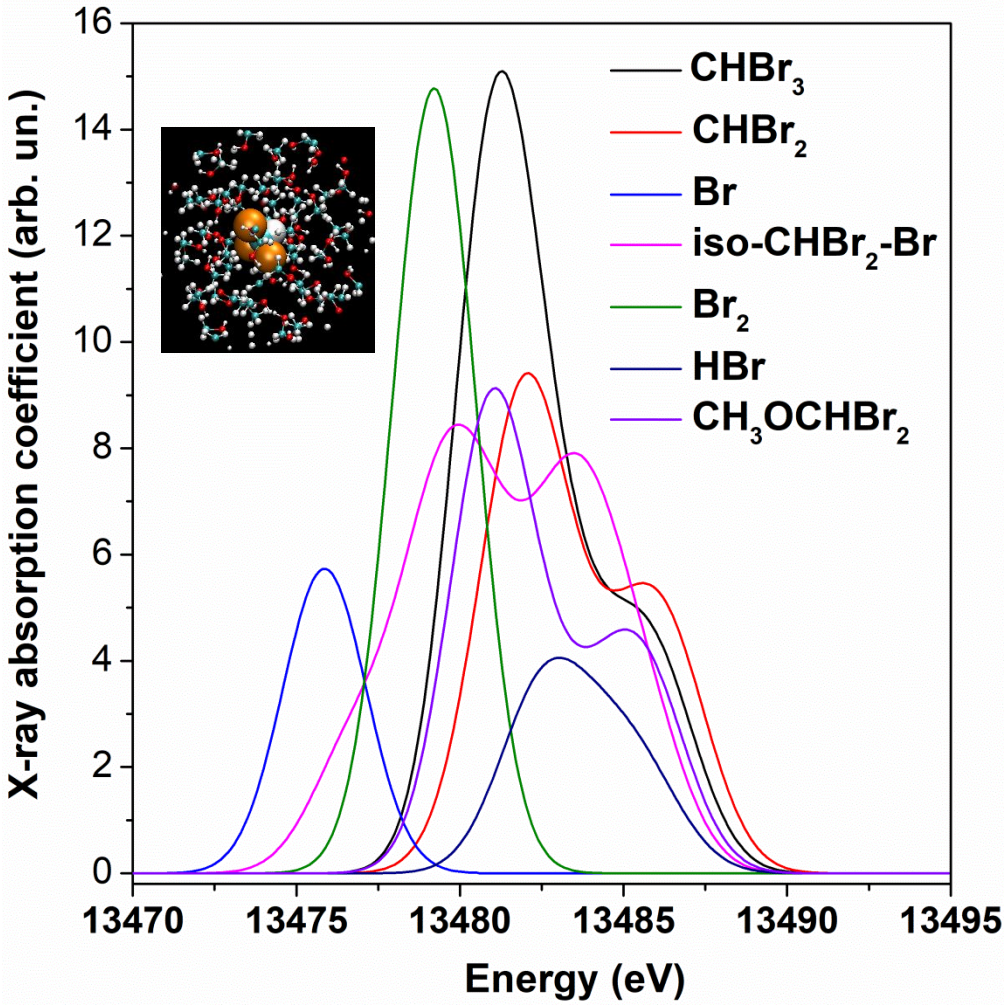

Figure S14. Calculated XANES spectra for $CHBr_3$ and putative intermediates in methanol. ORCA program suite was used to simulate the spectra. A solvation shell of 10 Å radius surrounding the $CHBr_3$ molecule, which corresponds to ~45 methanol molecules, was included in the calculation. The inset shows a snapshot of a $CHBr_3$ molecule and its solvation shell obtained from MD simulations. Br: *orange*, O: *red*, C: *cyan*, H: *white*.

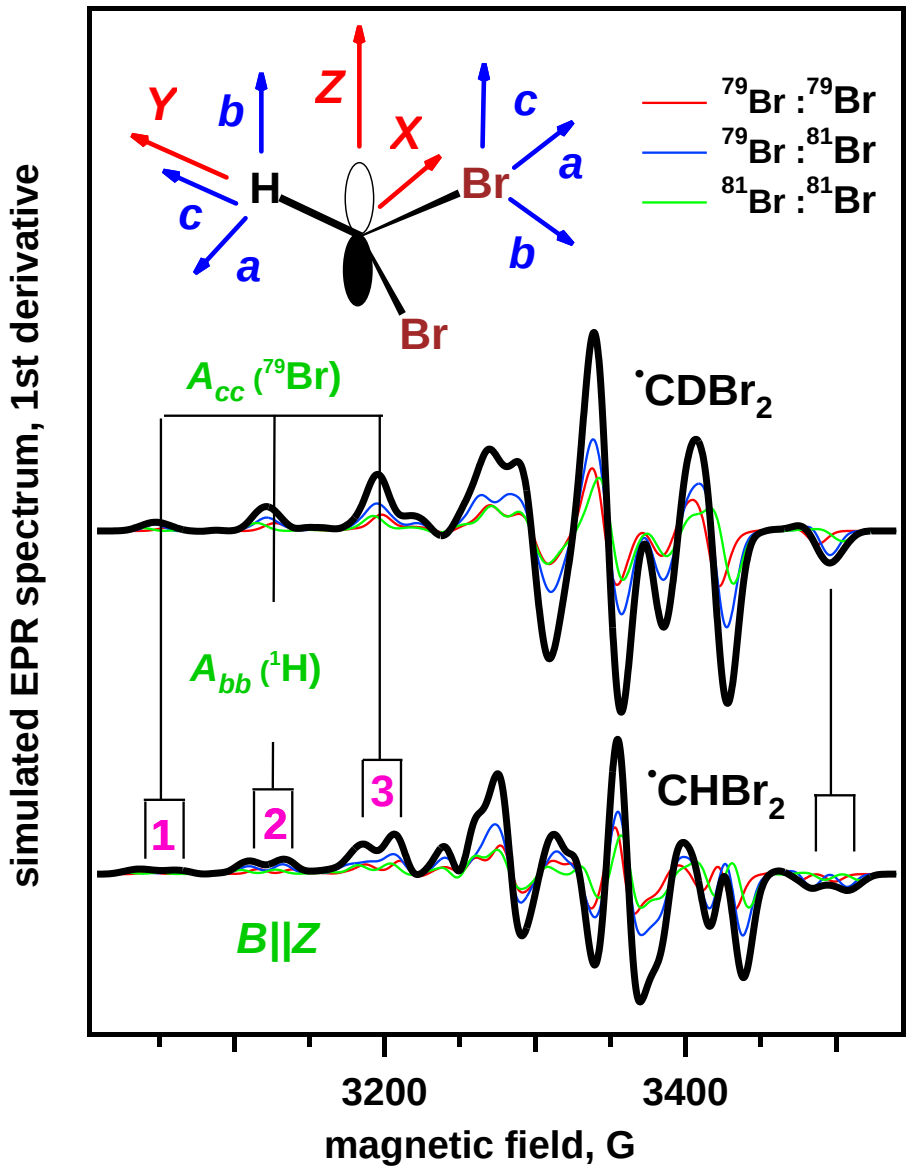

Figure S15. The simulated first-derivative EPR spectra of $CHBr_2$ and $CDBr_2$ radicals. In this calculation, the principal components of the ***g***-tensor were set to g_{xx}=2.0073, g_{yy}=2.040, and g_{zz}=2.061 (see the inset for the principal axes). The principal values of hfc tensors (with the principal axes *a*, *b*, and *c*) estimated by DFT are $A_{cc}(^{79}Br)$=(-39.3, -15.8, 73.9) G and $A_{bb}(^{1}H)$=(-36.2, -24.3, -9.7) G (see the inset for the principal axes). This EPR spectrum arises from the three isotopomers shown in the legend. In the low-field ***B***||*Z* component, three resonance lines (1, 2, and 3) arising from the coupling of the bromine nuclei to the electron spin in C *2p* orbital can be distinguished; the additional proton splitting is absent in $CDBr_2$.

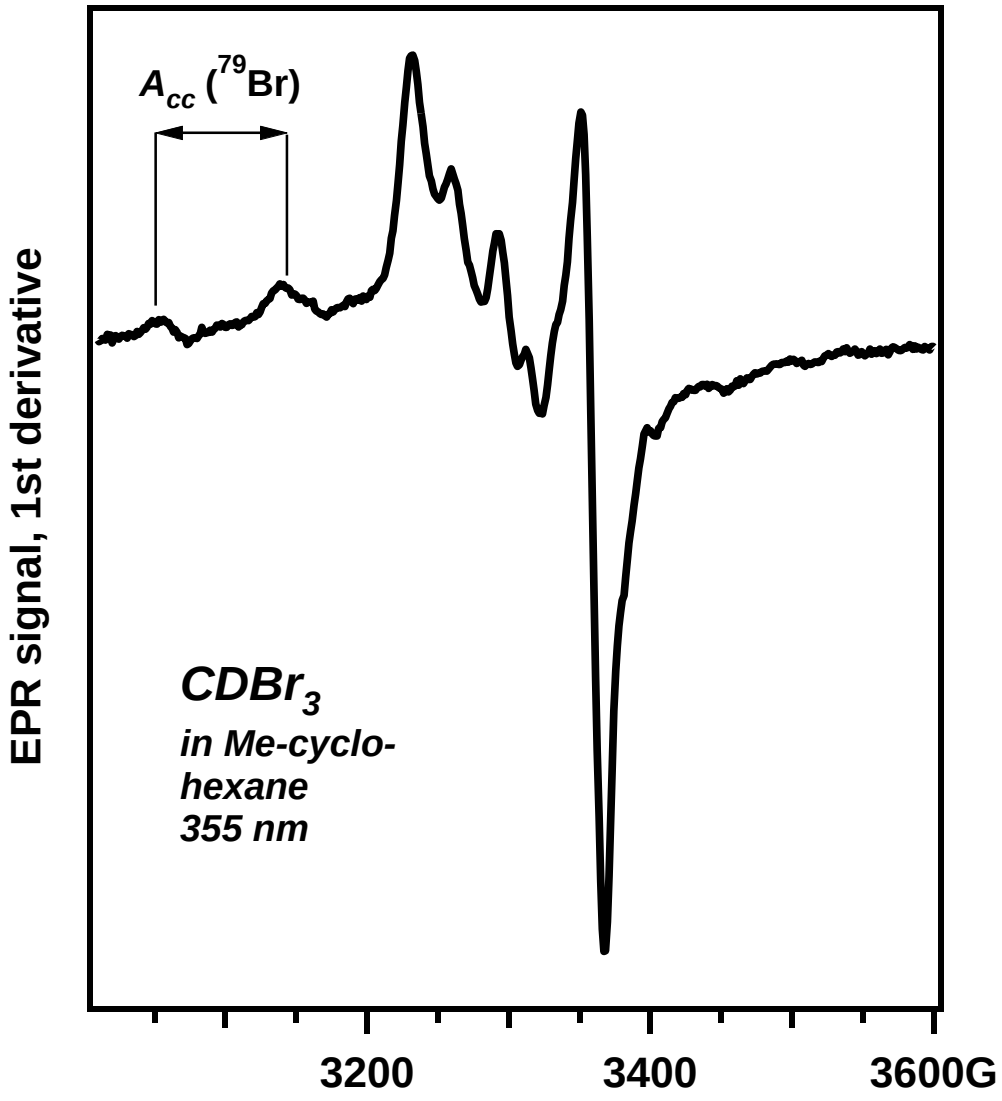

Figure S16. First-derivative EPR spectrum of $CDBr_2$ radical in methylcyclohexane. (355 nm laser photolysis of 1 wt% bromoform-*d* at 77 K, 8 G modulation, 9.445 GHz). The same EPR spectrum was observed after photolysis using an ultraviolet Xe arc lamp. The resonance lines of the Br atoms are not observed in this field range. The two low-field resonance lines (corresponding to $\boldsymbol{B}\|Z$) are from the bromine hfc's (see Figure S15) and correspond to $A_{cc}(^{79}\text{Br})\approx 88$ G (cf. Figure S15).

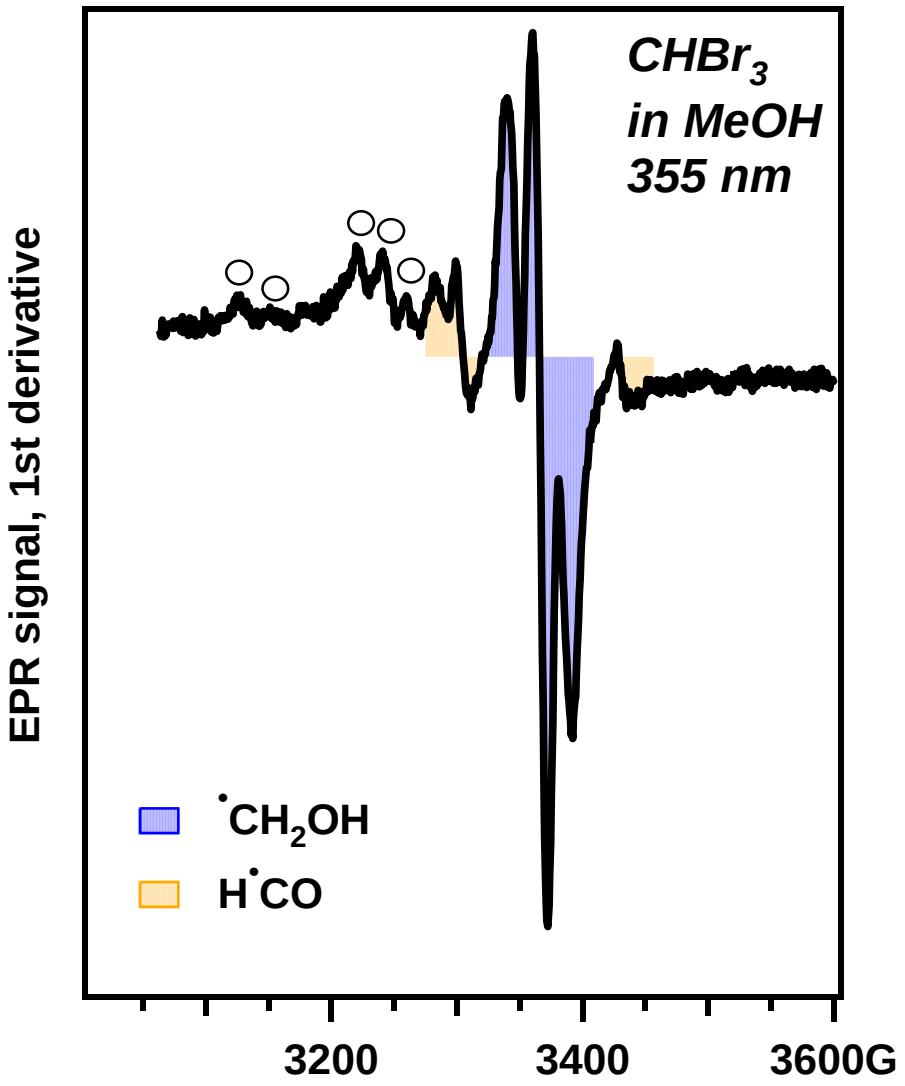

Figure S17. First-derivative EPR spectrum of laser photolyzed $CHBr_3$ in methanol-h_4. (355 nm photoexcitation, 25 mJ/pulse, 10 Hz, 15 min, 10 wt% solution, 5 G modulation, 9.441 GHz). The resonance lines indicated with open circles correspond to the $CHBr_2$ radical. The shadowed resonance lines correspond to CH_2OH (*blue*) and HCO (*brown*) radicals. The latter is the known product of secondary photolysis of CH_2OH radicals. Note the high yield of CH_2OH radicals.

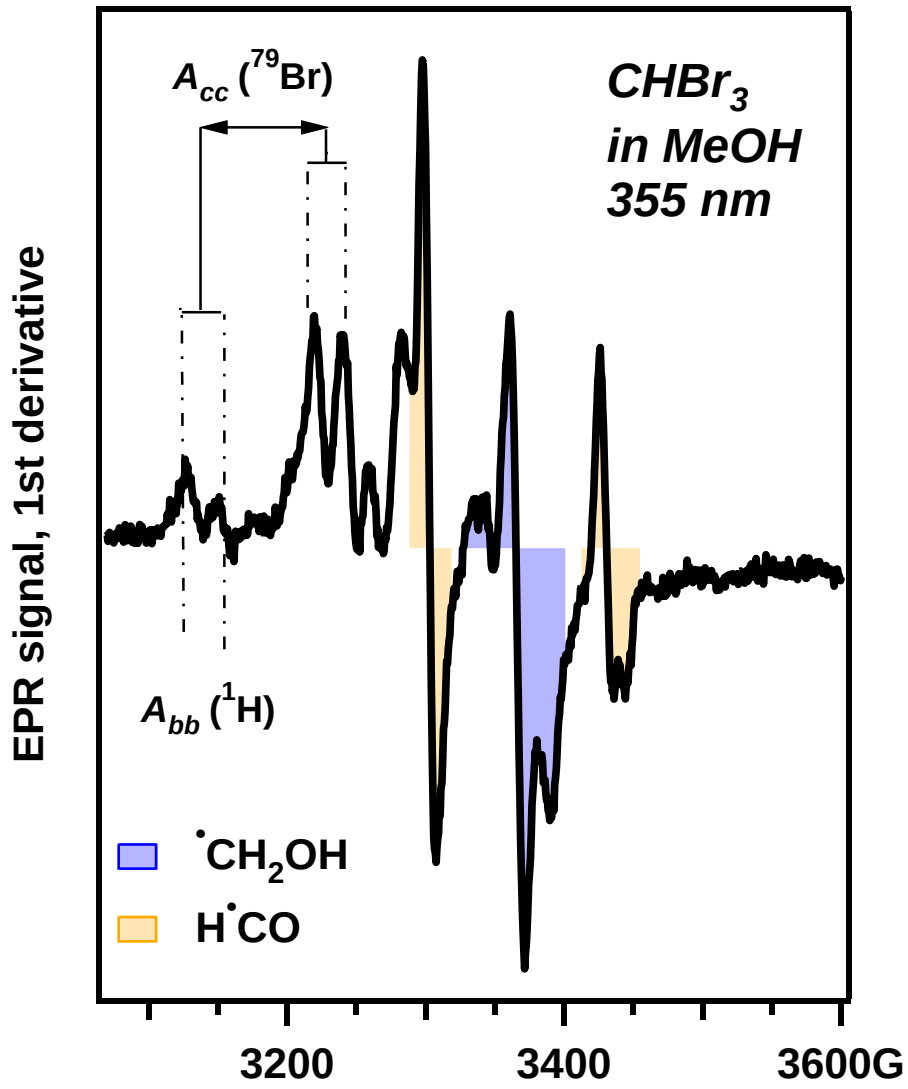

Figure S18. First-derivative EPR spectrum of the sample shown in Figure S17 after another 30 min of photolysis. Due to increased radical yield, the features of $CHBr_2$ radical are resolved more clearly. Both the bromine and proton splittings are seen in the low-field component with $A_{bb}(^1H)\approx23.5$ G and $A_{cc}(^{79}Br)\approx88$ G. Note the relative decrease in the concentration of CH_2OH and the increase in the concentration of HCO radical due to secondary photolysis of CH_2OH. The dots indicate the loci of the unpaired electron density.

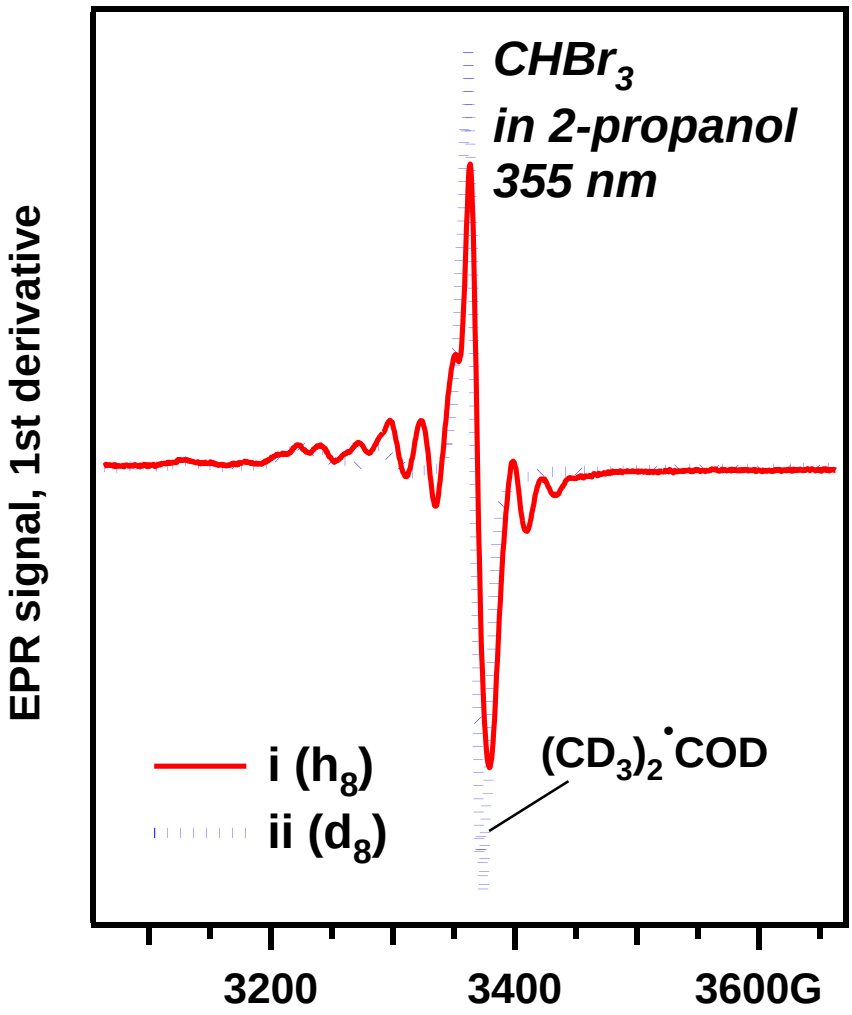

Figure S19. First-derivative EPR spectra of laser photolyzed $CHBr_3$ in 2-propanol for 15 minutes. (355 nm photoexcitation, 10 wt% solution, 10 G modulation, 9.442 GHz). Traces i and ii correspond to h_8 and d_8 isotopomers of the solvent, respectively. The additional resonance lines observed in trace i originate from the 2-propyl-h_7 radical, $(CH_3)_2COH$. These resonance lines are not observed in the 2-propyl-d_7 radical, $(CD_3)_2COD$, which has much smaller hfc's, so the EPR spectrum of this radical "collapses" to a single line.

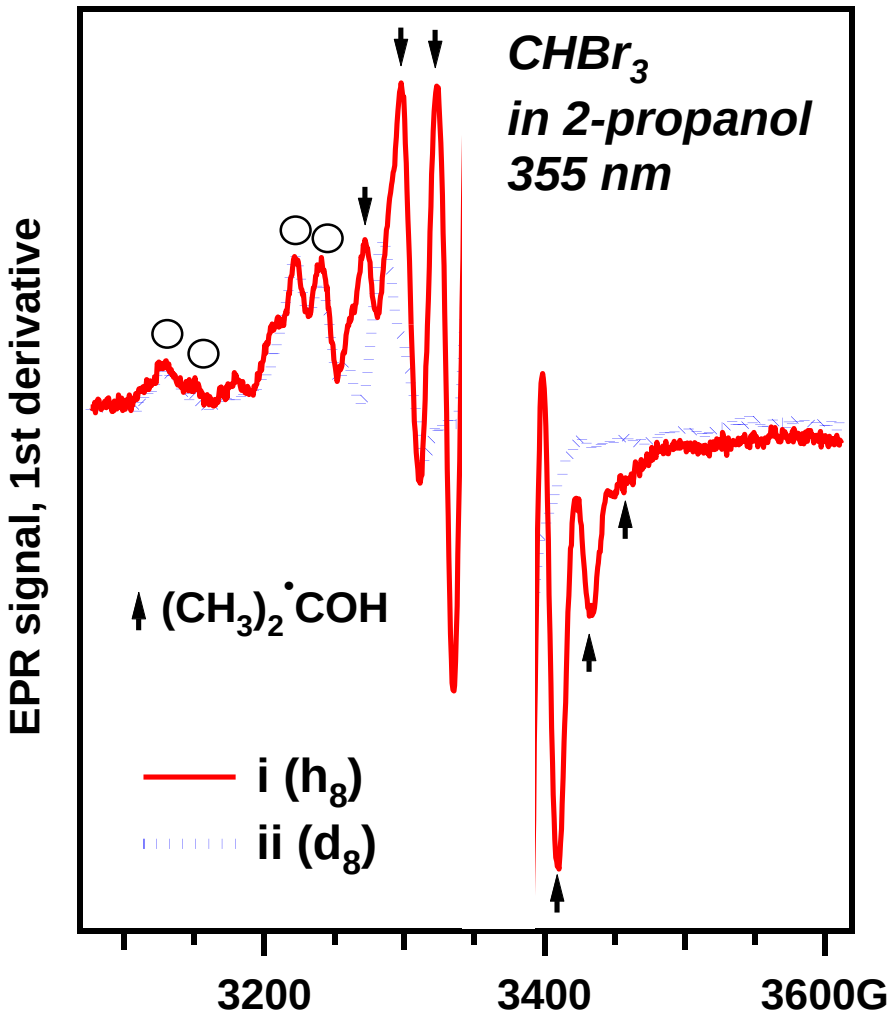

Figure S20. Vertically expanded view of the EPR spectra shown in Figure S19. The off-scale central line is not shown. The resonance lines indicated with open circles are from the $CHBr_2$ radical, and the resonance lines indicated with the vertical arrows in trace i are from the 2-propyl-h_7 radical (these resonances are not observed in the deuterated solvent).

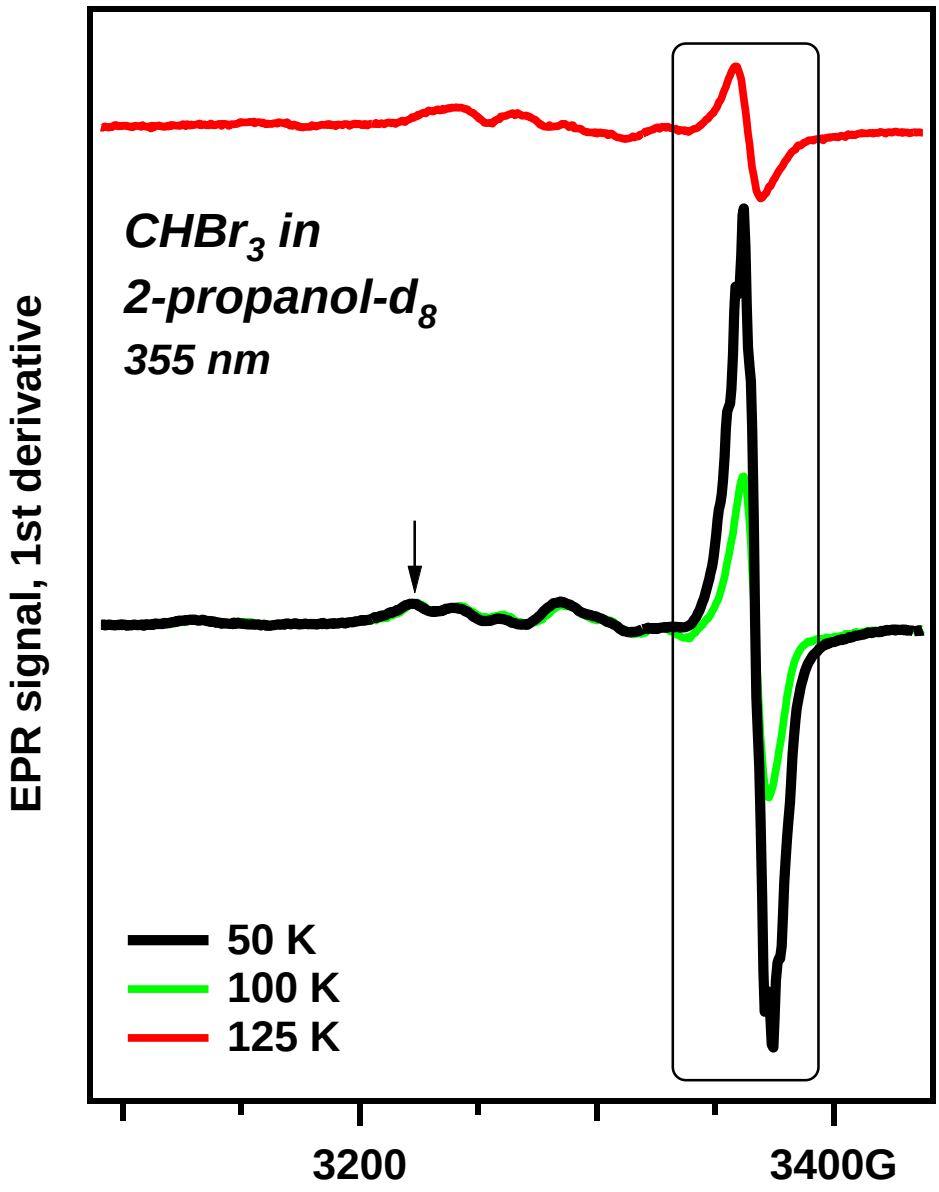

Figure S21. First-derivative EPR spectra of laser photolyzed $CHBr_3$ in 2-propanol-d_8 for 15 minutes. (355 nm, 10 wt% $CHBr_3$, 10 G modulation, 9.442 GHz). These EPR spectra were measured at 50, 100, and 125 K and normalized by the resonance line of $CHBr_2$ indicated with the vertical arrow. As temperature increases, the relative amplitude of the resonance line arising from the 2-propyl-d_7 radical decreases. The narrow line of the 2-propyl-d_7 radical (indicated with the rectangular frame) partially overlaps with the resonance line of $CHBr_2$ radical.

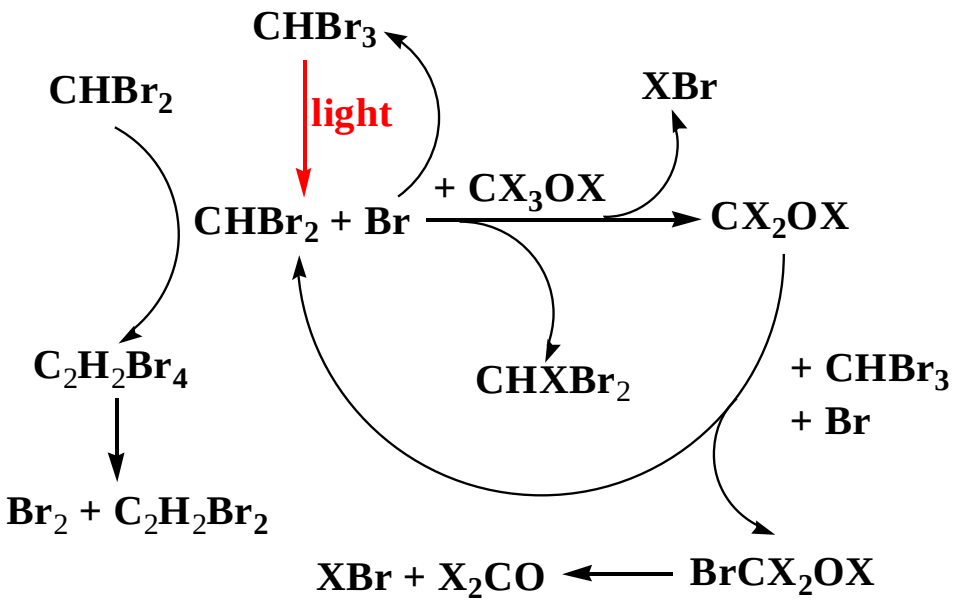

Figure S22. Chain reaction of dibromomethyl radical ($CHBr_2$) in methanol.

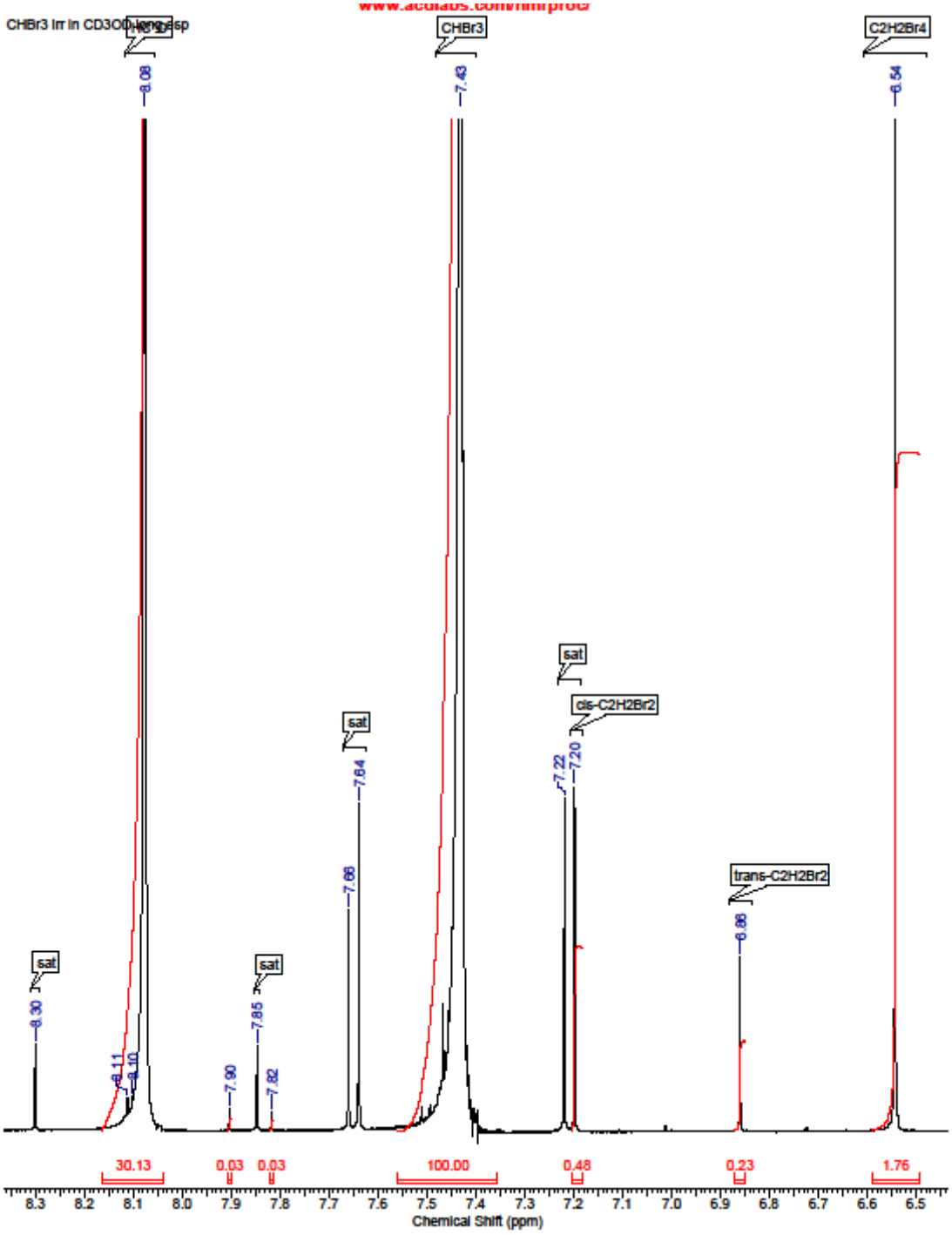

Figure S23. ^{1}H NMR spectrum of photolyzed bromoform (50 mM) in methanol-d_4. CH_2Br_2 is obscured by the solvent peak. Label "sat" indicates ^{13}C satellites of $CHBr_3$.

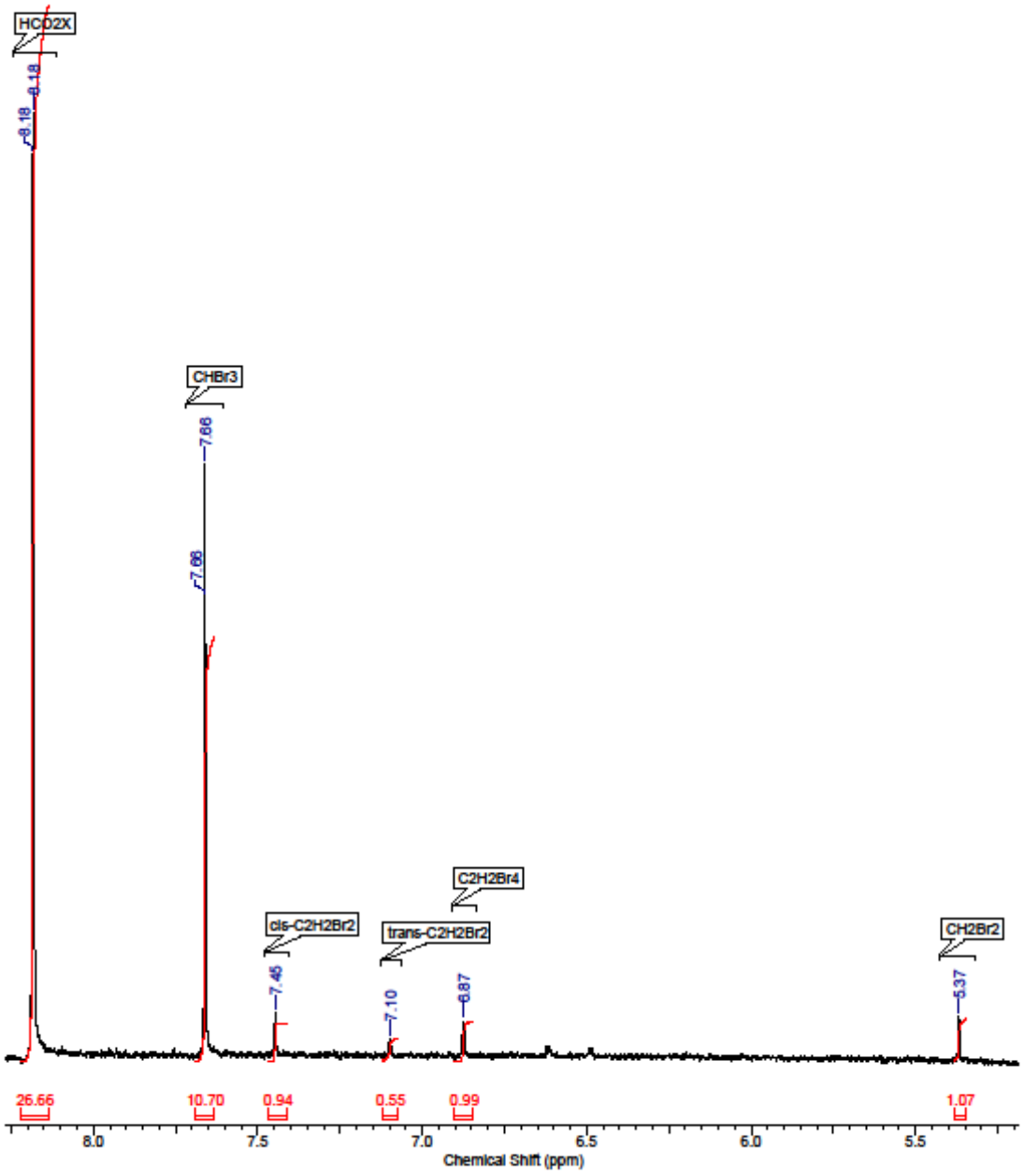

Figure S24. ^{1}H NMR spectrum of photolyzed bromoform in methanol-h_4. (50 mM $CHBr_3$, 1:10 v/v dilution with dimethylsulfoxide-d_6). Only in this mixed solvent, all four brominated products are observed simultaneously and quantified without interference from impurity and solvent resonances.

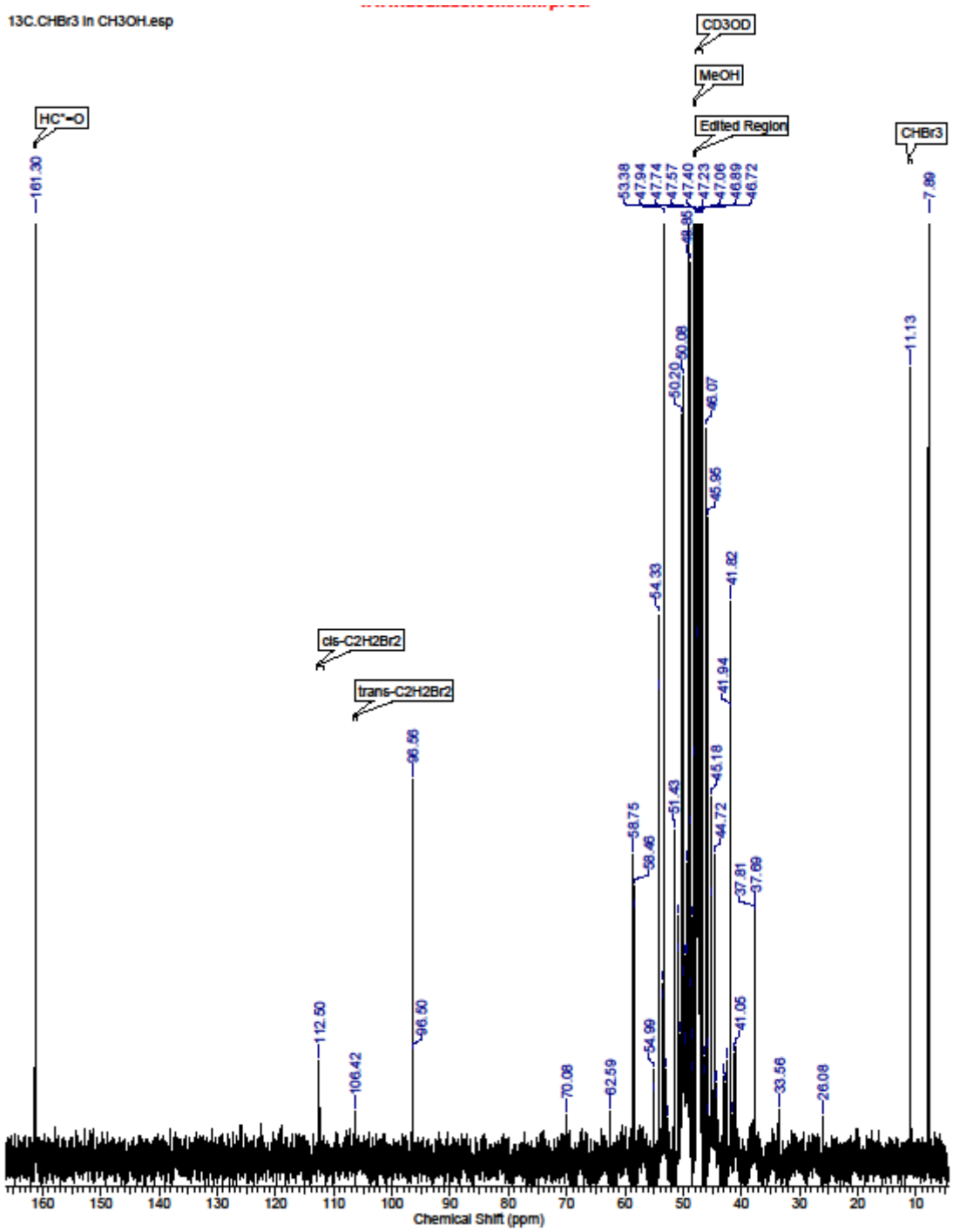

Figure S25. ^{13}C NMR spectrum of photolyzed bromoform in methanol-h_4. The solution contains 5 vol% CD_3OD for frequency locking. The large number of unattributed lines is from the impurities in the solvent.

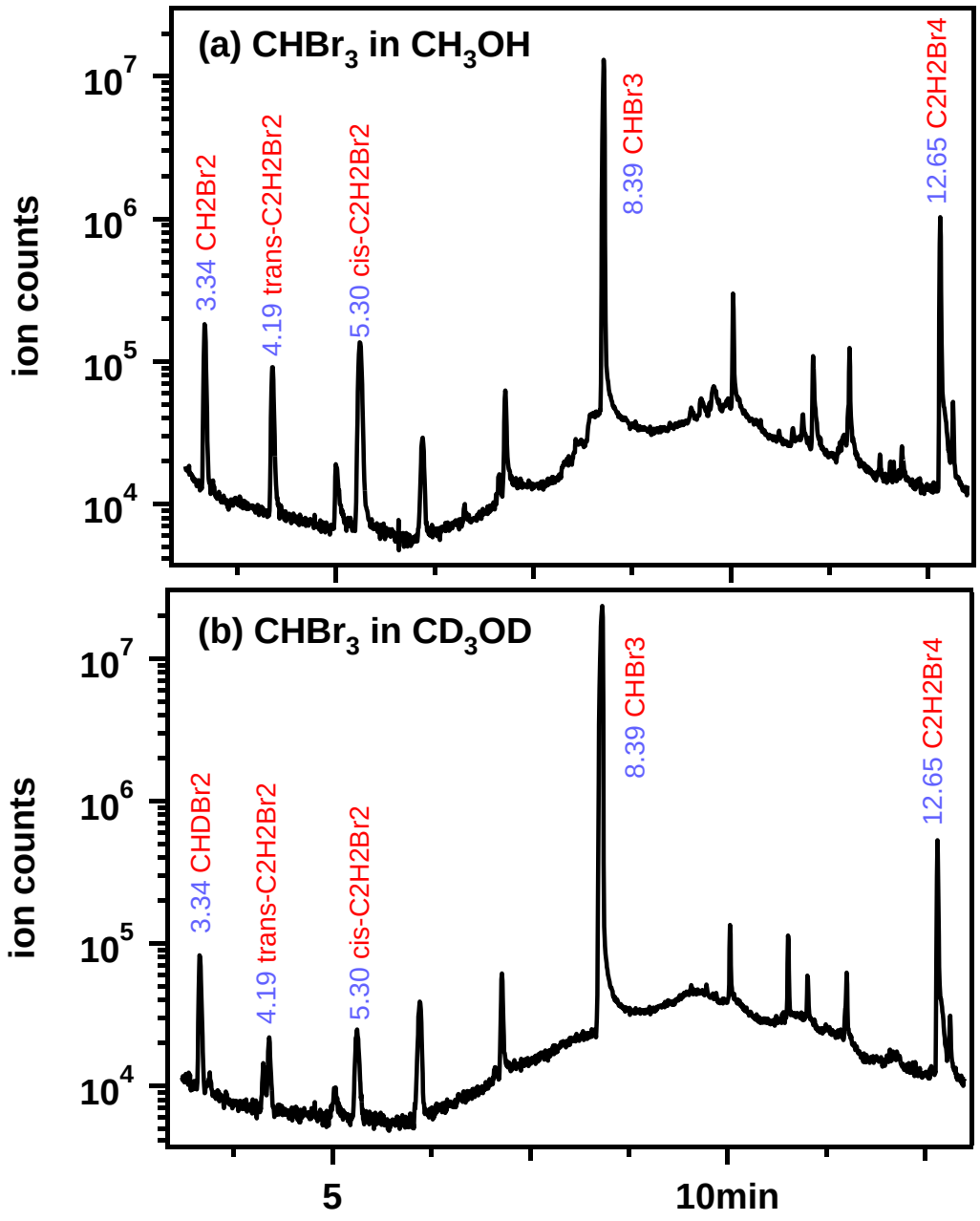

Figure S26. The gas chromatograms of photolyzed bromoform (50mM) in (a) methanol-h_4 and (b) methanol-d_4. Only brominated products are indicated; the retention time is given in blue, and the attribution is given in red. The unattributed peaks originate from solvent impurities and nonbrominated photoproducts.

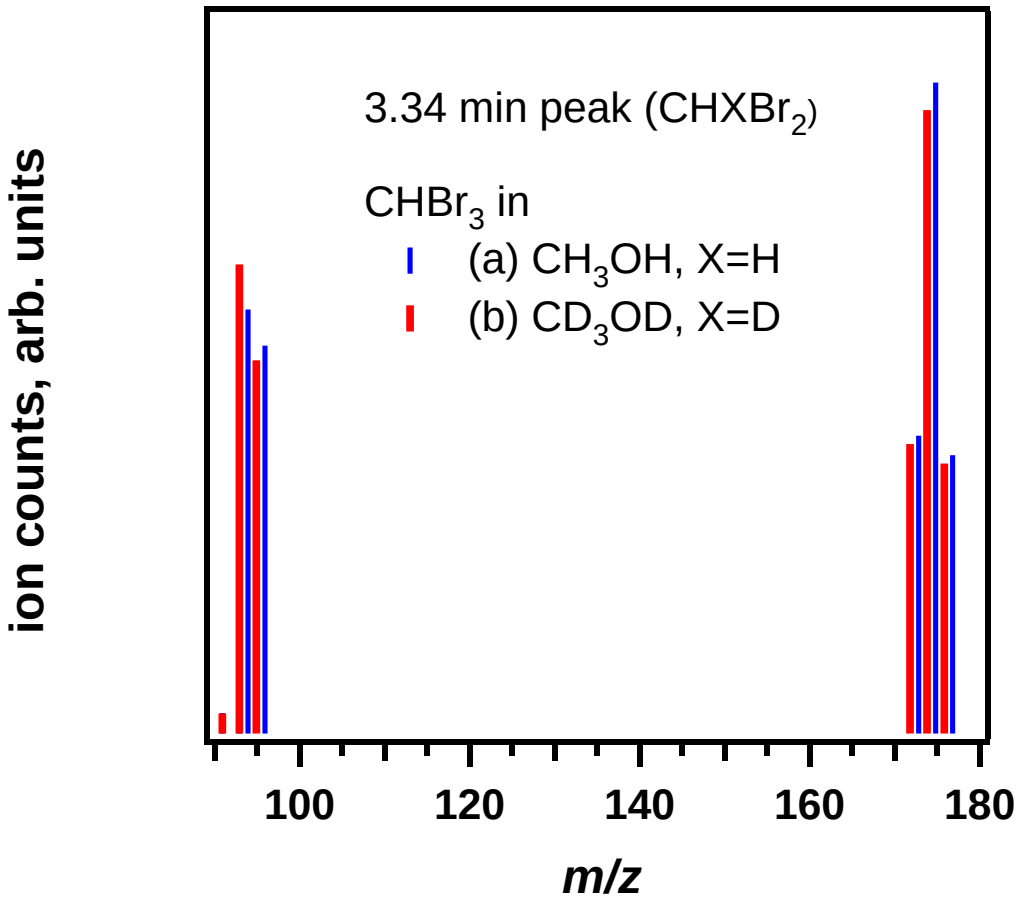

Figure S27. Mass spectra of dibromomethane generated from photolysis of 50 mM $CHBr_3$ (a) methanol-h_4 (*red*) and (b) methanol-d_4 (*blue*). The mass and Br loss fragment peaks are shifted by 1 a.m.u. when the photolysis is carried out in the deuterated solvent. This indicates the formation of $CHDBr_2$ via reaction S5.